Chemical Geology 264 (2009) 24–42

Contents lists available at ScienceDirect

Chemical Geology

journal homepage: www.elsevier.com/locate/chemgeo

In situ perovskite Sr–Nd isotopic constraints on the petrogenesis of the Ordovician Mengyin kimberlites in the North China Craton

Yue-Heng Yang [a], Fu-Yuan Wu [a,*], Simon A. Wilde [b], Xiao-Ming Liu [c], Yan-Bin Zhang [a], Lie-Wen Xie [a], Jin-Hui Yang [a]

[a] State Key Laboratory of Lithospheric Evolution, Institute of Geology and Geophysics, Chinese Academy of Sciences, P. O. Box 9825, Beijing 100029, China
[b] Department of Applied Geology, Curtin University of Technology, P. O. Box U1987, Perth, Western Australia 6845, Australia
[c] State Key Laboratory of Continental Dynamics, Department of Geology, Northwest University, Xi'an 750069, China

ARTICLE INFO

Article history:
Received 5 October 2008
Received in revised form 17 February 2009
Accepted 18 February 2009

Editor: R.L. Rudnick

Keywords:
Laser ablation analyses
Sr–Nd–Hf isotopes
Perovskite
Mengyin kimberlite
North China Craton

ABSTRACT

Precise Sr, Nd and Hf isotopic data are important indicators in deciphering the evolution of magmatic rocks and their source. However, such data are difficult to obtain for kimberlite, since these rocks are commonly contaminated by both crustal and mantle materials and also show extensive alteration and weathering following emplacement. In this study, numerous kimberlitic samples from Mengyin in northeast China were selected for U–Pb dating and Sr–Nd–Hf isotopic analysis of perovskite. *In situ* U–Pb analyses of fresh perovskite yield an age of 470 ± 4 Ma, which is considered the emplacement age of the Mengyin kimberlite. However, the altered perovskite shows Pb loss and yields Paleozoic-Mesozoic ages, indicating that perovskite is not as strongly resistant to isotopic modification as previously thought. *In situ* Sr–Nd isotopic analyses by laser ablation of perovskite grains collected from the main Mengyin kimberlite record uniform Sr and Nd isotopic compositions with an average initial $^{87}Sr/^{86}Sr$ ratio of 0.70371 ± 12 and $\varepsilon_{Nd}(t)$ value of 0.13 ± 0.22, which are identical, within uncertainties, to the values obtained by solution analyses. However, they are significantly different from comparable data obtained from whole rock samples, indicating that initial Sr–Nd isotopic ratios calculated from whole rock measurements on kimberlites are likely to record mixed isotopic signatures, due to crustal contamination and/or subsequent alteration. This conclusion is also supported by the Hf isotopic data for perovskite. Meaningful isotopic ratios for kimberlite can therefore only be obtained from single minerals such as pervoskite. The Mengyin samples investigated in this study have isotopic compositions similar to the Group I kimberlite, as defined in Southern Africa, and are interpreted to reflect derivation from a primitive mantle source. Combined with the fact that the Mengyin kimberlites were emplaced coevally with regional lithospheric uplift in the Ordovician at ~470 Ma, it is proposed that a mantle plume triggered kimberlite magmatism in this part of the North China Craton.

1. Introduction

Kimberlite is a unique ultramafic rock derived from either the lithosphere or sub-lithospheric mantle (Mitchell, 1986, 1995; Woolley et al., 1996) and can provide invaluable information about the composition and structure of that lithosphere (Mitchell, 1986). Based on mineralogical and petrological characteristics and Sr–Nd isotopic data, kimberlites can be divided into two main types; Group I (non-micaceous, with low initial Sr and high initial Nd isotope signatures) and Group II (phlogopite-bearing, with high initial Sr and low initial Nd isotope signatures) (Smith, 1983); a transitional type has also been reported (Becker and Le Roex, 2006). However, two important problems hamper the determination of kimberlite genesis. Firstly, kimberlite, by definition, contains abundant, variably-sized crustal and mantle xenoliths (Mitchell, 1986), which makes it difficult to determine the initial isotopic composition of the kimberlitic magma. Secondly, kimberlite is highly susceptible to alteration during both emplacement and by later weathering, due to its high content of volatiles and mantle minerals. Therefore, the combined effects of contamination and post-emplacement alteration limit the reliability of whole-rock isotopic analyses (Mitchell, 1986), and make these largely ineffective when trying to determine mantle sources (Heaman, 1989).

Fortunately, perovskite ($CaTiO_3$) can be used to circumvent many of the problems outlined above since it occurs mainly in the kimberlite groundmass and crystallized early in the magmatic history, along with ilmenite, rutile and magnesian chromite, and prior to crystallization of monticellite, phlogopite, serpentine and calcite (Mitchell, 1972, 1986; Thy et al., 1987). Therefore, perovskite has the potential to record the primary geochemical and isotopic signature of the magma, prior to any contamination and/or weathering. Furthermore, although perovskite is unstable in residual magmatic fluids (H_2O and CO_2) and is commonly resorbed and/or mantled by thin rims of rutile, it is

* Corresponding author. Tel.: +86 10 82998217; fax: +86 10 62010846.
E-mail address: wufuyuan@mail.igcas.ac.cn (F.-Y. Wu).

0009-2541/$ – see front matter © 2009 Elsevier B.V. All rights reserved.
doi:10.1016/j.chemgeo.2009.02.011

normally resistant to weathering (Mitchell, 1986). Thus perovskite tends to remain fresh when other constituents have been intensely altered. In addition, perovskite has high Sr and low Rb concentrations (Jones and Wyllie, 1984; Mitchell and Reed, 1988; Heaman, 1989), which make it suitable for obtaining initial Sr isotope ratios that can then be applied to decipher the petrogenesis and evolution of the kimberlite. In particular, the high Sr concentration, with low Rb (<2 ppm) and hence extremely low $^{87}Rb/^{86}Sr$ ratio (generally less than 0.001), makes pervoskite an excellent mineral for laser ablation analysis (Paton et al., 2007a,b). The obtained $^{87}Sr/^{86}Sr$ ratio can be considered as the initial Sr isotopic composition of the magma in which the perovskite crystallized, since the correction for *in situ* decay is negligible. Finally, according to available geochemical data (Mitchell, 1986; Mitchell and Reed, 1988; Heaman, 1989; Chakhmouradian and Mitchell, 2001), kimberlitic perovskites also contain high U, Th, Zr, Hf and REE concentrations, making it a potential mineral for U–Pb dating and Sm–Nd and Lu–Hf isotopic studies (Kramers and Smith, 1983; Allsopp et al., 1989; Smith et al., 1994; Kinny et al., 1997; Heaman et al., 2003, 2004; Cox and Wilton, 2006; Batumike et al., 2008).

The Mengyin kimberlites (~470 Ma) are important geological indicators that help constrain the tectonic evolution of the North China Craton (NCC) during the Phanerozoic (Fig. 1). The occurrence of diamond and mantle xenoliths in the main kimberlite (Shengli 1 pipe; Fig. 1b) indicate that the sub-continental lithospheric mantle (SCLM) underlying the NCC during the Paleozoic had a thickness of ~200 km (Chi and Lu, 1996; Griffin et al., 1998). Re–Os isotopic analyses on the contained mantle xenoliths yield an Archean age for this mantle lithosphere (Gao et al., 2002; Wu et al., 2003; Zhang et al., 2008). In contrast, samples of the SCLM underlying the NCC, as sampled by Cenozoic magmas, are characterized by melt depletion during the Proterozoic, and relatively recent juvenile additions to the lithosphere (Gao et al., 2002; Wu et al., 2003). These observations, coupled with geophysical evidence for relatively thin lithosphere at the present time, have led to the conclusion that the SCLM underlying the eastern part of the NCC was thinned and modified after the late Paleozoic (Menzies et al., 1993; Griffin et al., 1998; Wang et al., 1998; Yang et al., 2008a). However, the source of the Mengyin kimberlites is still unclear. Based on whole-rock Sr–Nd isotopic compositions, it has been suggested that they were derived from an enriched mantle (EMII) source in the SCLM and were transitional between Group I and II kimberlites of Smith (1983) (Luo et al., 1999; Zheng, 1999). However, extensive crustal contamination and later alteration make this questionable.

In this paper, we report a comprehensive series of Sr–Nd–Hf isotopic analyses of material obtained from the main Mengyin kimberlite at the former diamond mine (Fig. 1b,c). These include isotope dilution thermal ionization mass spectrometric (ID–TIMS) analyses of whole-rocks and perovskites and *in situ* laser ablation (LA) analyses of perovskites, performed to test if reliable Sr–Nd–Hf isotopic data can be obtained from kimberlitic perovskite.

2. Geological setting and sample descriptions

The NCC contains some of the oldest known rocks in the world, with 3.8 Ga crustal components exposed in the far north-east (Liu et al., 1992; Wu et al., 2008), although overall it is one of the youngest Archean cratons (Wu et al., 2005a) with abundant ages of ~2530 Ma. It forms the Chinese part of Sino-Korean Craton, covering most of North China with an area of approximately 1,500,000 km^2 (Fig. 1a). The Early Paleozoic Qilianshan Orogen and the Late Paleozoic Central Asian Orogenic Belt bound the craton to the west and the north, respectively, and in the south the Qinling-Dabie-Sulu ultrahigh-pressure metamorphic belt separates it from the South China Craton (Fig. 1a). Traditionally, the NCC was considered to be composed of a uniform early Precambrian (Archean-Paleoproterozoic) crystalline basement, overlain by younger cover (Huang, 1977). However, recent integrated lithological, structural, metamorphic and geochronological studies have led to a threefold tectonic division of the craton into Eastern and Western blocks, separated by the Paleoproterozoic Trans-North China Orogen (Zhao et al., 2005 and references therein).

Similar to other Archean blocks around the world, the NCC contains both greenstone belts and high-grade terrains, which were metamorphosed at ~2.5 Ga and subsequently cratonized at ~1.8 Ga by collision of the Eastern and Western blocks (Wu et al., 2005a; Zhao et al., 2005). Since ~1.8 Ga, the NCC has remained relatively stable and was covered by a thick sequence of Mesoproterozoic to Paleozoic sediments. In the Paleozoic, when the diamondiferous Mengyin and Fuxian kimberlites were emplaced in Shandong and Liaoning provinces, respectively (Zhang et al., 1989) (Fig. 1a), the NCC was characterized by thick carbonate sedimentation during the Cambrian–Early Ordovician. However, since Early–Middle Ordovician time (~465–470 Ma), a significant gap in sedimentation occurred until the Middle Carboniferous, coinciding with kimberlite emplacement. In the Mesozoic, extensive volcanic activity and granitoid emplacement occurred in the eastern NCC, possibly related to the interaction of the Eurasian and Pacific plates and resulting from lithospheric thinning (Wu et al., 2003, 2005b). During the Cenozoic, numerous alkaline basalts containing enclaves of mantle xenoliths and minor lower-crustal granulites were erupted throughout the central and eastern parts of the craton.

For this study, whole-rock samples containing perovskite were collected solely from the Mengyin kimberlites; unfortunately, perovskite is extremely rare in the diamondiferous kimberlite at Fuxian (Fig. 1a). At Mengyin, about 100 kimberlitic dykes and pipes have been identified (Fig. 1b, Wan, 1989; Chi and Lu, 1996), although pipe 1 (Shengli 1), located at N35°40′ and E117°47′, is the most important diamondiferous one in the area and was targeted for this study (Fig. 1c). This kimberlite contains a variety of crustal fragments, including limestone, gneiss and amphibolite (Wan, 1989; Dong, 1994; Chi and Lu, 1996), but some primary material is also present and shows much less crustal contamination. However, it is known that the Mengyin kimberlites contain exotic zircons with ages of ~2.5 Ga (Yin et al., 2005), indicating some crustal contamination. In addition, the main Mengyin kimberlite underwent extensive alteration, as indicated by alteration of garnet (Fig. 1d), olivine and pyroxene megacrysts.

Perovskite is relatively abundant in the kimberlite groundmass, with concentrations up to 5% (rarely up to 20%, Fig. 2a). Most grains are dark orange-brown in color with euhedral shapes and grain-sizes ranging between 30 and 200 μm (Fig. 2b). Many grains are homogeneous (Fig. 2c), although several show weak zoning in back-scattered electron (BSE) images (Fig. 2d) and others are weakly to strongly altered (Fig. 2g,h,l,n and o). Most perovskite occurs as individual grains, but it also co-exists with ilmenite, commonly enclosing spinel (Fig. 2e). In addition, perovskite also occurs as inclusions in ilmenite (Fig. 2f), indicating it crystallized slightly earlier than ilmenite, but later than spinel. Some grains are partially replaced by calcite (Fig. 2g) and titanite (Fig. 2h), although their original shapes are preserved as pseudomorphs (Fig. 2i–j). In sample MY31, many of these pseudomorphs are euhedral (Fig. 2k), but some are intensely altered and anhedral (Fig. 2l). In sample MY32, perovskites containing lower amounts of REE are less altered than those with high REE concentrations (Fig. 2m–o).

3. Analytical methods

Several kimberlite samples without visible crustal and/or mantle xenoliths were selected for whole-rock Sr–Nd–Hf isotopic analyses using the isotope dilution (ID–TIMS) method. Additional kimberlitic material was processed in order to obtain perovskite separates, which were also analyzed for Sr–Nd–Hf isotopes using the ID–TIMS

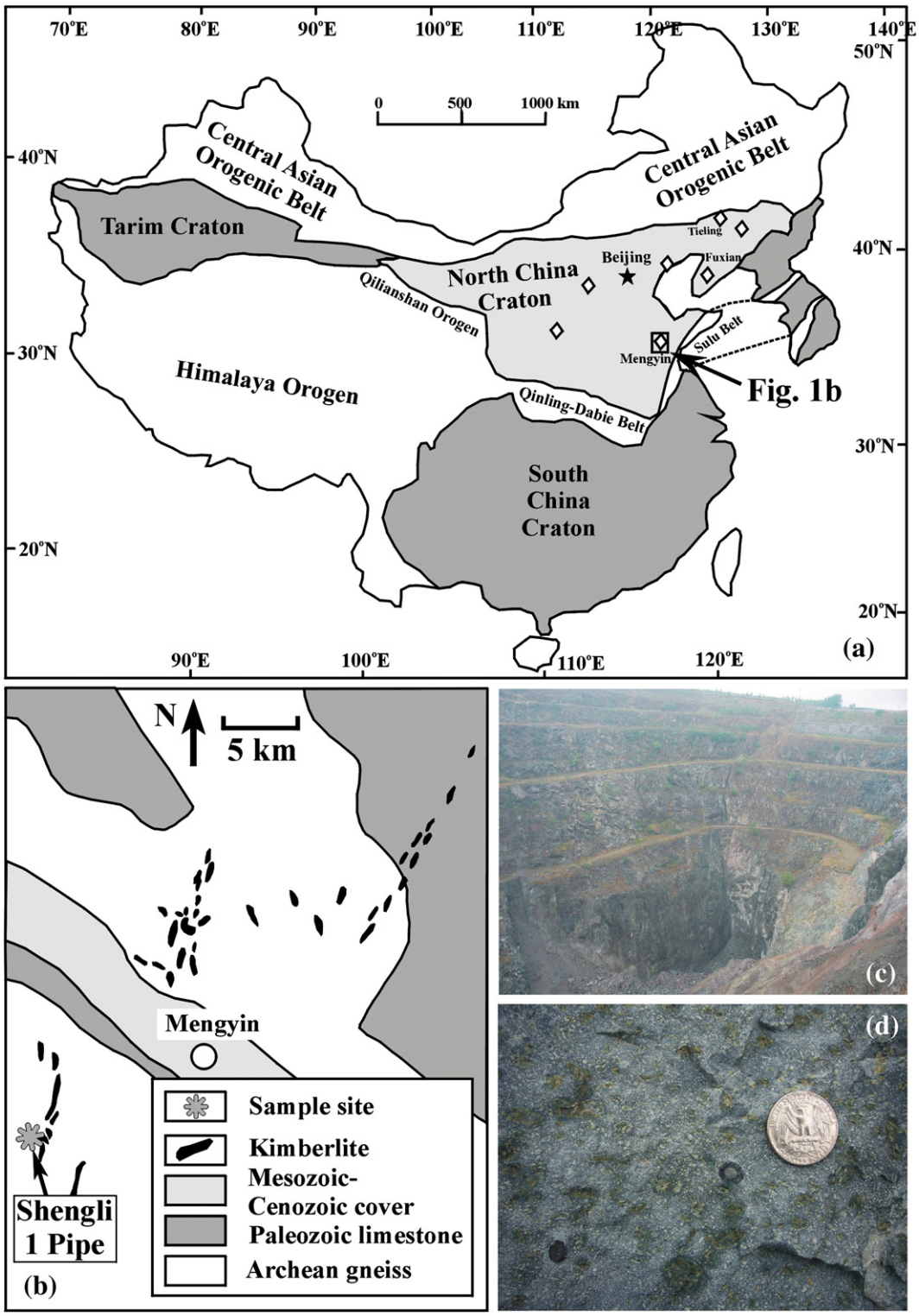

Fig. 1. (a) Simplified tectonic map of China, showing location of kimberlites, including diamondiferous ones mentioned in this study; (b) distribution of kimberlites at Mengyin in Shandong Province, North China Craton; (c) Former diamond mine (Shengli 1) at Mengyin; (d) Field photograph of Mengyin kimberlite showing pseudomorphed garnet megacrysts adjacent to the coin which is 22 mm in diameter.

Fig. 2. Pseudo-color back scattered electron (BSE) images of perovskites from the Mengyin kimberlite. (a) distribution of perovskite (green) with most having a grain-size of ~50 μm (sample MY19); (b) euhedral perovskite (sample MY15); (c) homogeneous perovskite (MY26); (d) zoning in perovskite (sample MY17); (e) crystallization sequence shown by early formation of euhedral and zoned spinel (Sp), enclosed by ilmenite (Ilm), and finally surrounded by perovskite (Pv) (sample MY12); (f) perovskite (Pv) inclusion in ilmenite (Ilm) (sample MY24); (g) slight alteration of perovskite around grain margin with presence of calcite (Cc) (sample MY21); (h) moderate alteration of perovskite with titanite (Titn) and high REE–enriched patches (sample MY27); (i) similar features as in (h) (sample MY21); (j) perovskite pseudomorph after intense alteration (sample MY21); (k) both euhedral and altered perovskites in sample MY31; (l) altered perovskite with little fresh residue material remaining, and REE-enriched patches (MY31); (m) weak alteration of perovskite with calcite (Cc) and REE-enriched patches around grain margin after weak alteration (MY32); (n) moderate alteration of perovskite with calcite (Cc) and olivine (Ol) around margins and extensive REE-enriched areas throughout the grain which shows after moderate alteration (sample MY32) and (o) intensive alteration of perovskite with high REE-enriched patches throughout crystal (MY32). (For interpretation of the references to colour in this figure legend, the reader is referred to the web version of this article.)

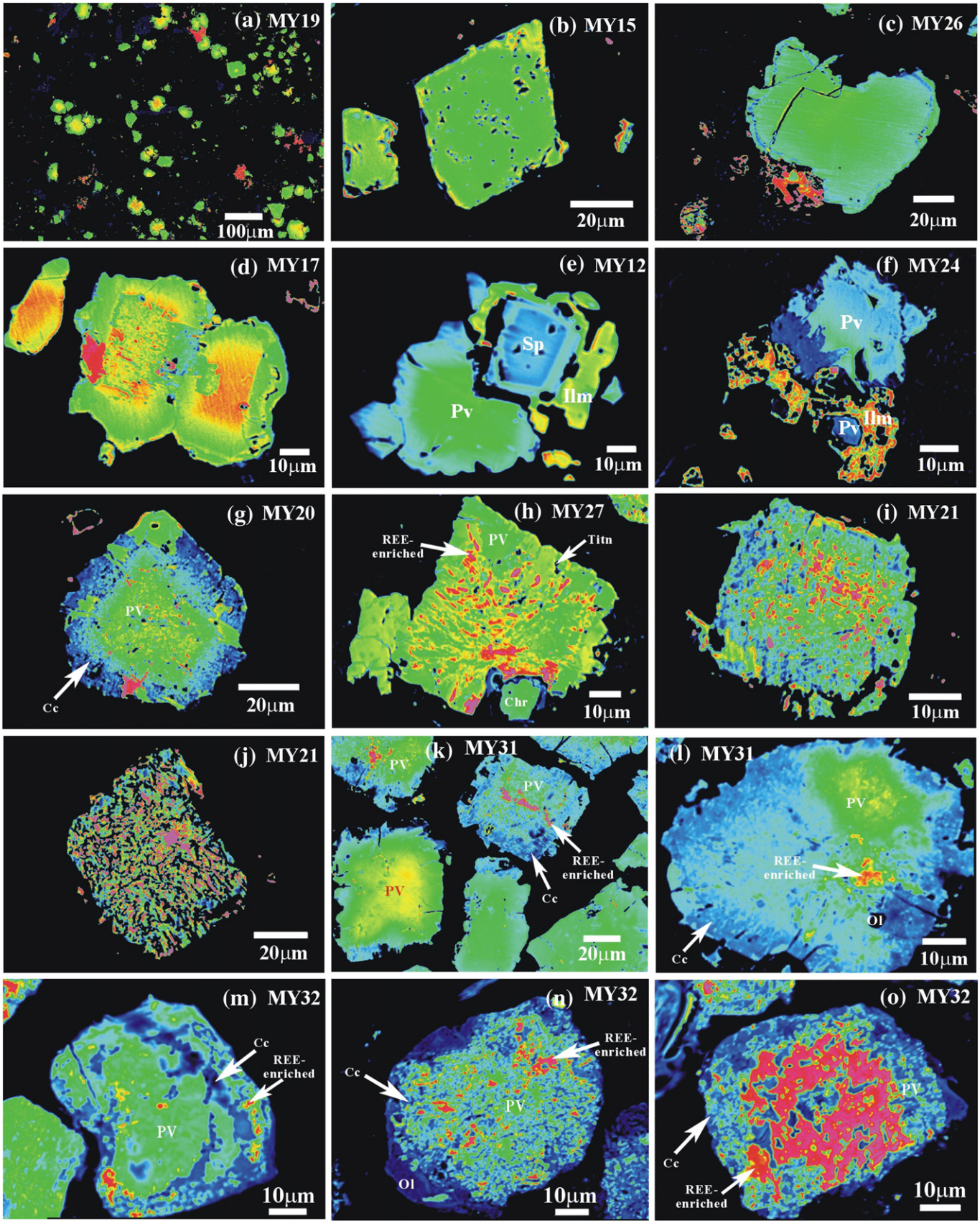
(a) MY19
100μm
(b) MY15
20μm
(c) MY26
20μm
(d) MY17
10μm
(e) MY12
Sp
Pv
Ilm
10μm
(f) MY24
Pv
Ilm
Pv
10μm
(g) MY20
PV
Cc
20μm
(h) MY27
REE-enriched
PV
Titn
Chr
10μm
(i) MY21
10μm
(j) MY21
20μm
(k) MY31
PV
PV
PV
REE-enriched
Cc
20μm
(l) MY31
PV
REE-enriched
Ol
Cc
10μm
(m) MY32
Cc
REE-enriched
PV
10μm
(n) MY32
REE-enriched
Cc
PV
Ol
10μm
(o) MY32
PV
Cc
REE-enriched
10μm

method. From this fraction, perovskite grains were also selected for *in situ* Sr–Nd analyses by laser ablation (LA), being first analyzed for major elements by electron microprobe and then by laser ablation inductively-coupled plasma mass spectrometry (LA–ICP–MS) for trace element compositions and U–Pb isotopes. All analyses were conducted at the Institute of Geology and Geophysics, Chinese Academy of Sciences.

3.1. Perovskite analyses for major and trace elements and U–Pb ages

Sample preparation for electron microprobe and subsequent LA–ICP–MS analyses of perovskite was relatively simple. Perovskite grains free of visible inclusions and major fractures were handpicked and embedded in epoxy and then polished to expose the grain centres. Major element compositions were obtained using a JEOL–JAX8100 electron microprobe with 15 kV accelerating potential and 12 nA beam current. Counting times were 20 s. Total iron is expressed as FeO. The analytical uncertainties are within 2% for TiO_2 and CaO, but ~10–20% for other elements due to their low concentrations.

Mineral trace element compositions (including REE) and U–Pb ages were conducted using LA–ICP–MS; detailed analytical procedures are provided in Yuan et al. (2004) and Xie et al. (2008). An ArF excimer laser ablation system (Geolas CQ) operated at 193 nm with a pulse width of ca. 15 ns was used for laser ablation analysis. In the first session of this study, 63, 94 and 127 μm spot sizes were applied, since ablation with bigger spots provides more material for more precise analysis. However, after updating the laser system (GeoLas PLUS) in June, 2007, 40 and 60 μm spot sizes were used, depending on the mineral grain-size, with similar precision. The laser repetition rate was 2–10 Hz depending on the signal intensity, with fluency of ~20 J/cm^2. The ablation depth is estimated to be ~30–40 μm. With a 40 μm spot size and 4 Hz repetition rate, the volume of ablated material is estimated to be ~200,000 μm^3. Helium gas was flushed into the sample cell to minimize aerosol deposition around the ablation pit and to improve transport efficiency (Eggins et al., 1998; Jackson et al., 2004).

The trace element and U–Pb analyses were conducted using an Agilent 7500a ICP–MS. During laser ablation, the sensitivity of ^{238}U using the NIST SRM 610 standard glass was 14,000 cps/ppm (40 μm spot, 10 Hz repetition rate). The mass stability was better than 0.05 amu/24 h. Before routine analysis, the Pulse/Analogy (P/A) factor of the detector of the ICP–MS was corrected. It was also necessary to optimize instrumental parameters using a tuning solution in order to make the productivity of oxide (CeO^+/Ce^+) and doubly charged Ce^{++}/Ce^+ less than 0.5% and 3%, respectively, and sensitivity better than 20×10^6 cps/ppm for ^{89}Y. The background of ^{204}Pb and ^{202}Hg was less than 100 cps because of the high purity of the argon and helium gas.

ICP–MS measurements were carried out using time-resolved analysis and peak hopping at one point per mass. The dwell time for each isotope was set at 6 ms for Si, Ca, Ti, Rb, Sr, Ba, Nb, Ta, Zr, Hf and REE, 15 ms for ^{204}Pb, ^{206}Pb, ^{207}Pb and ^{208}Pb and 10 ms for ^{232}Th and ^{238}U. Every 5 sample analyses were followed by one standard zircon 91500 and one NIST SRM 610 measurement. Each spot analysis consisted approximately of a 30 s background acquisition and 40 s sample data acquisition. $^{207}Pb/^{206}Pb$, $^{206}Pb/^{238}U$, $^{207}Pb/^{235}U$ ($^{235}U = {}^{238}U/137.88$) and $^{208}Pb/^{232}Th$ ratios were corrected by using zircon 91500 as an external standard. The fractionation correction and results were calculated using GLITTER 4.0 (GEMOC, Macquarie University; van Achterbergh et al., 2001). All the measured isotope ratios of zircon 91500 during sample analysis were regressed and corrected using recommended values; the standard deviations of these values were set at 2%. After obtaining the Pb isotopic ratios, the ^{207}Pb method was applied for common Pb corrections using the two-stage model of Stacey and Kramers (1975) (see also Williams, 1998), and the $^{206}Pb/^{238}U$ weighted ages were calculated using ISOPLOT 3.0 (Ludwig, 2003). Errors on individual analyses are based on counting statistics and are at the 1σ level, but errors on pooled ages are quoted at 2σ or 95% confidence level. Trace element concentrations were calculated using GLITTER 4.0 and calibrated using ^{40}Ca as an internal standard and NIST SRM 610 as an external reference material. The analytical uncertainties are mostly within 10%.

3.2. Sr–Nd–Hf analyses by isotope dilution

Chemical separation was achieved by conventional ion-exchange techniques. Pure perovskite without any visible impurities was selected by hand picking. Prior to sample digestion, pervoskite separates were washed in a sonic bath for 30 min in Millipore water (MQ) and then in diluted HCl for 10 min. The perovskite was then rinsed with MQ water before being transferred to vials. Kimberlite whole-rock powder (ca. 100 mg) and pervoskite crystals (ca. 5–10 mg) were dissolved with a mixed spike (^{87}Rb–^{84}Sr, ^{149}Sm–^{150}Nd and ^{176}Lu–^{180}Hf) in 2.5 ml concentrated HF, 0.2 ml HNO_3 and $HClO_4$ in steel-jacketed Teflon bombs placed in an oven for a week at 190 °C. Following dissolution and spike-sample homogenization, each sample was dried down at high temperature (fuming $HClO_4$) on a hot plate; then the mixture was treated with 6 M HCl, evaporated to dryness, and taken up in 3 M HCl before chemical separation. The treatment with 6 M HCl is necessary to completely convert fluorides into chlorides (Münker et al., 2001).

The first stage was the separation of Lu and Hf using Eichrom Ln-spec resin (100–150 μm, 2 ml), modified from the procedure of Münker et al. (2001). The major element and L(M)REE fraction was collected using 3 M HCl for further purification. After collecting the Lu (+Yb) fraction using 4 M HCl, the columns were rinsed with 6 M HCl to effectively remove any remaining Lu and Yb before collection of the Hf fraction. This was followed by separation of Ti from Hf using an $HCl + H_2O_2$ mixture. In addition, the Hf fraction was eluted with 2 M HF. The second stage employed traditional cation exchange chromatography for Rb and Sr purification (Richard et al., 1976). The L(M)REE fraction eluted with 6 M HCl was further purified using another Eichrom Ln resin (100–150 μm, 2 ml) with 0.25 M HCl for Nd and 0.40 M HCl for Sm, modified from the technique of Pin and Zalduegui (1997).

Rb–Sr and Sm–Nd isotopes were analyzed using a Finnigan MAT 262 thermal ionization mass spectrometer (TIMS). Procedural blanks were less than 100 pg for Rb and Sr, and 50 pg for Sm and Nd. $^{87}Sr/^{86}Sr$ and $^{143}Nd/^{144}Nd$ ratios were normalized to $^{86}Sr/^{88}Sr = 0.1194$ and $^{146}Nd/^{144}Nd = 0.7219$ using the exponential law. In the course of this study, the analyses of NBS987 and Ames Nd standard yielded $^{87}Sr/^{86}Sr = 0.710244 \pm 20$ ($n = 20$, 2SD) and $^{143}Nd/^{144}Nd = 0.512145 \pm 15$ ($n = 20$, 2SD), respectively. Isotopic analyses of Lu and Hf were determined using a Neptune multi-collector inductively coupled plasma mass spectrometry (MC–ICP–MS) and followed the methods of Vervoort et al. (2004). Typical analytical blanks were less than 50 pg for Hf and 10 pg for Lu. Hafnium isotope ratios were corrected for instrumental mass bias to $^{179}Hf/^{177}Hf = 0.7325$ using the exponential law. During this study the measured $^{176}Hf/^{177}Hf$ of JMC-475 was 0.282163 ± 14 ($n = 7$, 2SD). During the period of data acquisition, USGS reference materials BCR-1 and BHVO-2 were also processed for Sr–Nd–Hf isotopes, and gave ratios of 0.705012 ± 11 and 0.703495 ± 11 for $^{87}Sr/^{86}Sr$, 0.512626 ± 10 and 0.512987 ± 10 for $^{143}Nd/^{144}Nd$ and 0.282875 ± 10 and 0.283095 ± 8 for $^{176}Hf/^{177}Hf$, respectively, which are identical, within error, to the recommended values (Weis et al., 2005, 2006, 2007).

3.3. In situ Sr–Nd isotopic analyses by laser ablation

3.3.1. Instrumentation

The *in situ* Sr–Nd analyses were carried out using a Neptune MC–ICP–MS. The detailed descriptions of the instrument and laser ablation system are presented in Wu et al. (2006), so only a brief outline is given here. The mass spectrometer is a double-focusing multi-collector ICP–MS and has the capability of high mass resolution

measurements in multiple collector mode. The present instrument is equipped with eight motorized Faraday cups and one fixed central channel, where the ion beam can be switched between Faraday and SEM detector. The external precision of the measurements is further improved by utilizing a rotating amplifier concept, in which all Faraday cups are sequentially connected to all amplifiers, cancelling out any gain calibration errors.

3.3.2. In situ Sr isotopic analyses

The Sr isotopic data were acquired in static, multi-collector mode with low resolution using nine Faraday collectors, and the mass configuration array from ^{83}Kr to ^{88}Sr, monitoring Kr and Rb, which is identical to the technique of Ramos et al. (2004). Prior to analysis, collectors were aligned using a tuning solution which contains Rb, Sr, Er, and Yb. An aliquot of 200 ppb NBS 987 (NIST SRM 987) was used regularly for controlling the quality and optimizing the operation parameters, including the torch position, the Ar flow rate and the ion lens focus, to get maximum sensitivity. During the past two years, the average $^{87}Sr/^{86}Sr$ and $^{84}Sr/^{86}Sr$ ratios are 0.710251 ± 21 and 0.05649 ± 10 ($n=68$, 2SD), respectively. These values are identical to those recommended by Thirlwall (1991) and Balcaen et al. (2005) with a variation of 0.002%.

During laser ablation analysis, various interferences have to be evaluated. Prior to every analytical session, the Neptune MC–ICP–MS was always set-up to monitor Kr in the Ar gas after optimization, especially when a new liquid Ar tank was installed. During analyses, 50 s measurement of the gas blank was carried out prior to ablation in order to correct Kr, similar to the method employed by Ramos et al. (2004). The natural Kr ratios of $^{83}Kr/^{84}Kr = 0.20175$ and $^{83}Kr/^{86}Kr = 0.66474$ are used for overlap correction. The natural ratio of $^{85}Rb/^{87}Rb = 2.5926$ was used for isobaric correction of Rb by the exponential law, assuming that rubidium has the same mass discrimination as strontium (Ehrlich et al., 2001). Our experiments indicate that the small fraction of Rb in the Sr fraction, with Rb/Sr ratio less than 0.02 ($^{87}Rb/^{86}Sr \sim 0.06$), can be effectively corrected. No correction was applied for the interference of Ca argide/dimmer species since it has been demonstrated that this interference is negligible (e. g., Ehrlich et al., 2001; Fortunato et al., 2004; Ramos et al., 2004; Vroon et al., 2008). This was also supported by our experiments, where there were no differences in the $^{84}Sr/^{86}Sr$ and $^{87}Sr/^{86}Sr$ ratios between the chemically Sr-purified and unpurified corals (see below). Interferences from Fe dioxides, and Ga and Zn oxides, are not considered in this study, due to their low signals during analysis. However, interference from the doubly-charged rare earth elements (REEs) is not negligible when perovskite was ablated for Sr and Nd isotopic measurements, due to the high concentrations of REEs. Based on the method proposed by Ramos et al. (2004), we monitored the presence of $^{167}Er^{2+}$, $^{171}Yb^{2+}$ and $^{173}Yb^{2+}$ at masses 83.5, 85.5 and 86.5. Then the contributions of $^{168}Er^{2+}$ and $^{168}Yb^{2+}$ to ^{84}Sr, $^{170}Er^{2+}$ and $^{170}Yb^{2+}$ to ^{85}Rb, $^{172}Yb^{2+}$ to ^{86}Sr, $^{174}Yb^{2+}$ to ^{87}Sr ($+^{87}Rb$), and $^{176}Yb^{2+}$ to ^{88}Sr were calculated according to the isotopic abundances of Er and Yb (Chartier et al., 1999; Vervoort et al., 2004). However, no corrections for $^{176}Lu^{2+}$ and $^{176}Hf^{2+}$ on ^{88}Sr were made in this study since their signal intensities are low. Ramos et al. (2004) demonstrated that the measured Sr isotopic ratios of NBS987 did not change when JMC475 Hf solution is added, which is also verified by our experiment with a mixed solution of NBS987, Merk Nd and JMC475 Hf. Combined with the fact that Mengyin perovskites have only about 0.5 ppm of Lu, it is concluded that interferences of $^{176}Lu^{2+}$ and $^{176}Hf^{2+}$ on ^{88}Sr are negligible.

Before sample analyses, modern coral (*Porites*) and an in-house perovskite standard (MY12) were used to evaluate the reliability of the laser ablation analyses, the calibration technique and matrix-matched effect. During data reduction, the effects of interfering elements were accounted for in the order Kr, Yb^{2+}, Er^{2+} and Rb. One hundred and twenty analyses of *Porites*, and forty-one analyses of perovskite MY12 yield average $^{87}Sr/^{86}Sr$ values of 0.709179 ± 54 (2SD) and 0.703652 ± 80 (2SD), respectively, which is identical to the values of 0.709176 ± 16 (2SD, $n=64$) and 0.703655 ± 16 (2SD, $n=2$) obtained by the solution method.

3.3.3. In situ Nd isotopic analyses

The laser ablation Nd isotope technique is similar to that for Sr described above. Before analysis, a standard Nd solution was used to calibrate the instrument. Using the exponential law for mass bias correction and assuming $^{146}Nd/^{144}Nd = 0.7219$, the average $^{143}Nd/^{144}Nd$ ratios for the La Jolla Nd standard solution over a two-year period is 0.511849 ± 0.000014 (2SD, $n=68$), which is identical, within error, to the recommended range of 0.511856–0.511858 by MC–ICP–MS (Vance and Thirlwall, 2002).

For laser ablation analyses, the spot size was 40–60 μm with a 4–10 Hz pulse rate. As in all laser ablation methodologies, great care must be taken to avoid or mitigate the effects of isobaric interferences. For *in situ* Nd isotopic analyses, the interferences are principally caused by Ce (^{142}Ce on ^{142}Nd) and Sm (^{144}Sm on ^{144}Nd). Since Ce and Nd have almost identical geochemical characteristics to the LREE, the higher the Nd concentration, the higher the Ce concentration in natural geological materials. Our work indicates that the influence of Ce on Nd isotopic analysis is insignificant when the Ce/Nd ratio is 3, which is the normal valve in natural geological materials (Yang et al., 2007). However, the most crucial aspect during *in situ* Nd isotope measurement is how to precisely determine the isobaric interference of ^{144}Sm on ^{144}Nd, especially determination of the mass bias of Sm (β_{Sm}) (Foster and Vance, 2006; Foster and Carter, 2007; McFarlane and McCulloch, 2007). In this study, the β_{Sm} value was obtained directly from the $^{147}Sm/^{149}Sm$

Table 1
Chemical compositions of the standard perovskites (Ice River and Tazheran).

	Ice river	1SD	Tazheran	1SD
Major elements (wt.%)				
SiO_2	0.00	0.01	0.00	0.00
TiO_2	54.86	0.51	55.18	0.25
Al_2O_3	0.25	0.03	0.19	0.02
FeO	1.01	0.11	1.13	0.06
NiO	0.01	0.02	0.02	0.02
MgO	0.01	0.01	0.02	0.02
CaO	38.77	0.70	40.51	0.27
MnO	0.01	0.02	0.01	0.01
Na_2O	0.53	0.08	0.25	0.03
K2O	0.00	0.00	0.00	0.00
Total	95.47	1.99	97.30	0.42
Trace and rare earth elements (ppm)				
Rb	0.18	0.03	0.24	0.26
Sr	2376	106	48	3
Ba	4.5	1.7	3.7	3.0
Nb	7196	397	3780	265
Ta	745	149	215	48
Zr	169	14	2648	222
Hf	4.8	0.4	160	12
U	149	26	1470	69
Th	1869	663	912	230
Pb	41	9.3	142	11
La	7220	599	3259	192
Ce	14912	2001	10315	537
Pr	1604	251	1291	71
Nd	6101	952	5072	283
Sm	836	81	781	46
Eu	212	14	111	7.1
Gd	425	28	424	28
Tb	47	3.3	61	3.8
Dy	197	14	311	17
Ho	27	2.4	51	3.1
Er	47	5.0	105	6.0
Tm	4.3	0.6	12	0.6
Yb	20	3.0	63	3.2
Lu	1.8	0.3	6.4	0.4
Y	445	43	692	36

ratio on the sample itself and then applied in the isobaric interference correction of ^{144}Sm on ^{144}Nd, following the method proposed by McFarlane and McCulloch (2007). We also used the ^{147}Sm/^{149}Sm ratio of 1.08680 (Dubois et al., 1992) and ^{144}Sm/^{149}Sm ratio of 0.22332 (Isnard et al., 2005), as determined by MC–ICP–MS, in data reduction (Yang et al., 2008b). Furthermore, the stable ^{145}Nd/^{144}Nd ratio was used to evaluate the feasibility of our method since it has a constant value of 0.348415 obtained by TIMS (Wasserburg et al., 1981). In order to evaluate measurement and matrix-matched effects, in-house standards of apatite (AP1) and perovskite (MY12) were analyzed, and yielded average ^{143}Nd/^{144}Nd ratios of 0.511342 ± 31 (2SD, n = 90) and 0.512229 ± 40 (2SD, n = 15), respectively, which agree well with 0.511334 ± 10 (2SD, n = 8) and 0.512230 ± 13 (2SD, n = 2), obtained by the purified solution method of MC–ICP–MS analysis. In addition, the

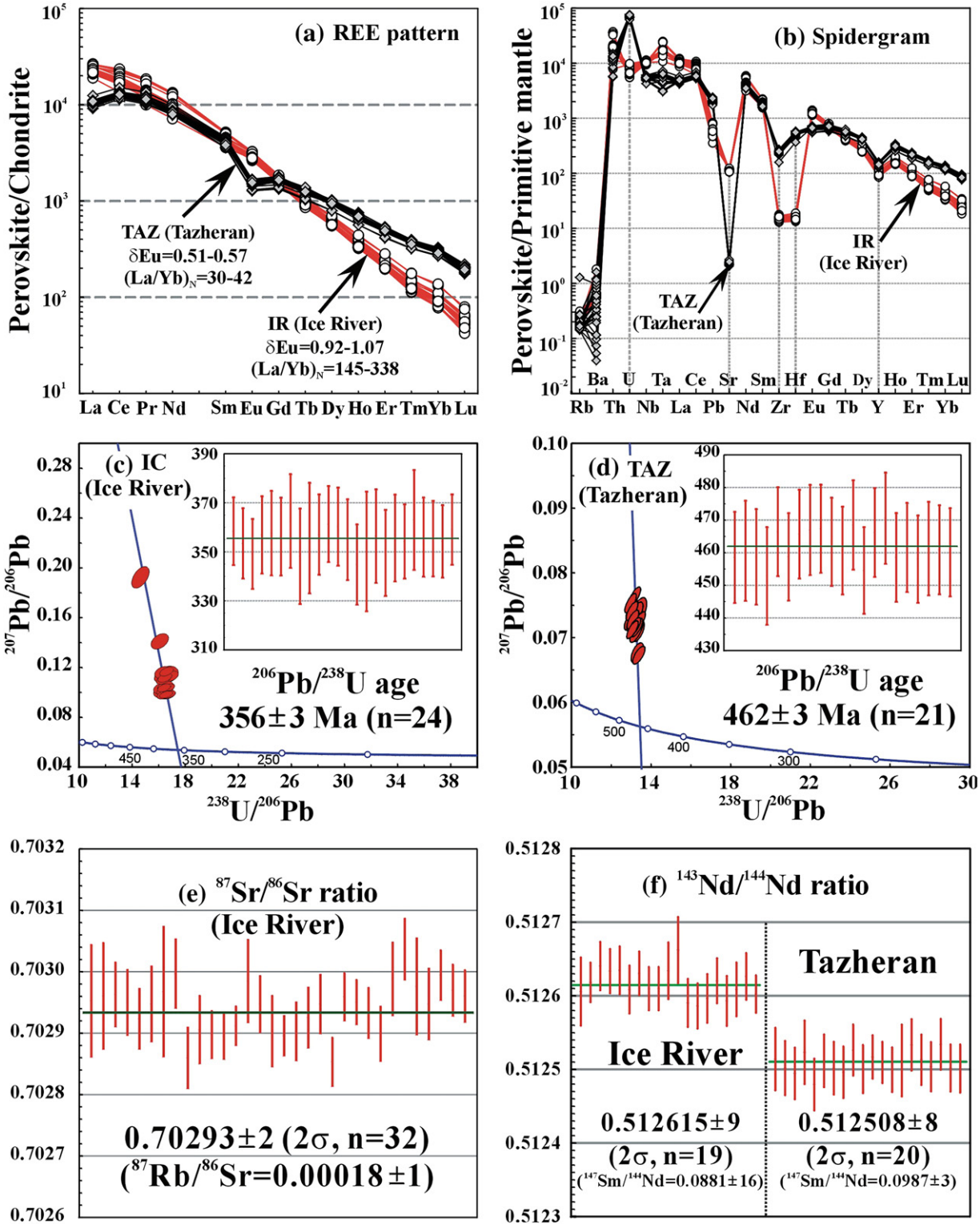

Fig. 3. Analytical results of the perovskite standards (IR: Ice River, TAZ: Tazheran). (a) Chondrite-normalized REE patterns; (b) Primitive mantle normalized plot, (c) Concordia plot for the Ice River perovskite, (d) Concordia plot for the TAZ perovskite, (e) ^{87}Sr/^{86}Sr data for the Ice River perovskite, and (f) ^{143}Nd/^{144}Nd data for the Ice River and TAZ perovskite.

average $^{145}Nd/^{144}Nd$ ratios of 0.348424 ± 19 (2SD) and 0.348419 ± 28 (2SD) are identical to the recommended value of 0.348415. Our experiments on standard glass NIST SRM 610, which has Sm and Nd concentrations of 441–460 and 429–442 ppm (Rocholl et al., 2000), respectively, with a Sm/Nd ratio of ~1.04 and a $^{143}Nd/^{144}Nd$ ratio of 0.511908–0.511927 (Woodhead and Hergt, 2001; Foster and Vance, 2006), indicate that reliable $^{143}Nd/^{144}Nd$ ratios can be obtained even when Sm/Nd is close to unity, although the Sm/Nd ratio of most natural geological materials is approximately 0.2–0.3. For REE-enriched minerals like apatite, titanite, allanite, xenotime, fluorite, monazite and perovskite, reliable Nd isotope data can be obtained using a spot size of 20 μm if they have Nd concentrations of ~1000 ppm (Yang et al., 2008b).

3.4. In situ analyses of perovskite standards

In order to check the reliability of our analytical techniques, perovskite standards IR and TAZ were selected for analyses. The IR sample was collected from the Ice River alkaline–ultramafic intrusion in southeastern British Columbia. The host rock is ijolite consisting of nepheline, clinopyroxene and perovskite, with accessory apatite, ilmenite, melanite and titanite. It is used as a U–Pb standard in numerous laboratories and has a recommended $^{206}Pb/^{238}U$ age of 356.5 ± 1.0 Ma ($^{206}Pb/^{238}U$ ratio of 0.05685 ± 17) (Heaman, 2009). Using laser ablation and applying the ^{207}Pb correction, Simonetti et al. (2008) obtained a weighted $^{206}Pb/^{238}U$ age of 352.5 ± 3.7 Ma. According to the data reported by Heaman (2009), this mineral also contains high Sr and REE elements, suitable for laser Sr–Nd isotopic analyses. TAZ perovskite is used as a U–Pb standard at Curtin University of Technology for SHRIMP analyses. It is from the Tazheran skarn deposit in the Lake Baikal area of eastern Siberia. Although no chemical compositional data are available, previous TIMS analyses indicated that this standard is nearly concordant with a concordia age of 463 Ma ($^{206}Pb/^{238}U$ ratio of 0.074465) (Kinny et al., 1997).

Our analyses indicate that the above two standards show very different compositions (Table 1). The IR standard is homogeneous in BSE images with low concentrations of U (149 ppm), Pb (41 ppm), Zr (169 ppm), Hf (4.8 ppm, Zr/Hf = 35) and Nb (7196 ppm), but high Sr (2376 ppm), Ta (745 ppm, Nb/Ta = 10), Th (1869 ppm, Th/U = 13). The chondrite-normalized REE pattern is highly fractionated without any Eu anomaly ($(La/Yb)_N$ = 145–338, Eu* = 0.92–1.07, Fig. 3a). In the spidergram, this standard shows significant depletions of Rb, Sr, Zr, Hf and Y (Fig. 3b). In contrast, the TAZ standard shows local compositional banding and dense fractures, and has the following values: U (1470 ppm), Pb (142 ppm), Zr (2648 ppm), Hf (160 ppm, Zr/Hf = 17), Sr (48 ppm), Ta (215 ppm, Nb/Ta = 18) and Th (912 ppm, Th/U = 0.6). In the chondrite-normalized REE diagram, it shows less fractionation of LREE to HREE, with significant La and Ce depletions and a negative Eu anomaly ($(La/Yb)_N$ = 30–42, Eu* = 0.51–0.57, Fig. 3a). Similar to the IR perovskite, this standard is also depleted in Rb, Sr, Zr, Hf and Y, but enriched in U (Fig. 3b).

Twenty-four and 21 U–Pb analyses were conducted on the IR and TAZ standards, respectively, and yield weighted $^{206}Pb/^{238}U$ ages of 356 ± 3 and 462 ± 3 Ma, applying the ^{207}Pb correction method (Fig. 3c

Table 2
Chemical composition of perovskites from the Mengyin kimberlites.

Element	MY6	MY12	MY15	MY17	MY19	MY20	MY21	MY24	MY26	MY27	MY28	MY30	MY31	MY32
Major elements (%)														
Spot number	N = 7	N = 7	N = 7	N = 8	N = 6	N = 7	N = 8	N = 7	N = 10	N = 7	N = 8	N = 10	N = 10	N = 5
Alteration	No	No	No	No	No	Yes	Yes	No	No	Yes	No	No	Yes	Yes
SiO_2	0.09	0.25	0.11	0.57	0.14	2.37	3.55	1.46	3.40	1.66	1.73	2.36	1.94	2.98
TiO_2	53.29	52.99	53.93	57.24	53.61	57.44	57.74	55.44	50.41	55.86	52.38	50.84	56.77	17.65
Al_2O_3	0.44	0.43	0.42	0.45	0.31	0.51	0.06	0.42	0.72	0.30	0.34	0.38	0.25	0.05
MnO	0.01	0.02	0.01	0.05	0.01	0.04	0.00	0.12	0.00	0.00	0.01	0.07	0.41	0.11
MgO	0.09	0.10	0.08	0.15	0.09	0.11	0.27	0.07	0.56	0.17	0.23	0.42	0.11	0.34
FeO	1.39	1.29	1.31	0.99	1.31	0.85	0.64	1.06	1.49	1.01	1.43	1.41	1.04	0.58
CaO	34.69	35.18	35.65	25.07	35.12	22.63	10.80	27.51	33.92	29.05	33.64	33.03	25.60	37.00
Na_2O	0.56	0.59	0.49	0.35	0.65	0.54	2.24	0.37	0.62	0.24	0.75	1.23	0.46	0.18
K_2O	0.06	0.09	0.07	0.06	0.06	0.13	0.48	0.05	0.12	0.04	0.11	0.30	0.09	0.09
Total	90.62	90.94	92.06	84.93	91.31	84.69	75.89	86.50	91.79	88.42	90.59	90.26	86.78	58.95
Trace and rare earth elements (ppm)														
Spot number	N = 7	N = 26	N = 7	N = 8	N = 6	N = 17	N = 14	N = 20	N = 19	N = 16	N = 20	N = 20	N = 20	N = 20
Rb	3.81	0.84	1.24	1.11	0.60	1.45	0.49	2.00	2.37	1.91	1.48	1.91	0.44	2.72
Sr	2204	2424	2361	1284	2441	585	503	1684	2321	1062	2155	2294	1145	620
Ba	93.8	81.4	63.6	71.2	112	146	298	64.3	111	154	82.5	88.4	333	96.6
Pb	160	116	138	60.9	121	81.5	74.8	76.4	76.1	166	106	96.3	68.3	65.1
Th	6309	4185	5452	3316	4608	5667	2421	3384	2919	16595	3740	3569	4830	4789
U	104	104	120	115	122	143	95.6	83.8	116	277	110	116	103	408
Nb	4889	5078	5079	5844	5292	7528	6043	5417	6652	14038	5429	6680	5782	6948
Ta	1026	814	984	779	830	1015	633	730	706	2649	912	757	1031	680
Zr	1224	1600	1496	2353	881	3355	2550	1989	2453	2150	1354	2089	1565	1049
Hf	68.2	68.7	72.9	88.5	45.1	99.5	73.6	68.1	83.3	110	70.4	72.2	65.9	25.7
La	9934	9165	9824	9081	9676	11605	8095	7913	8844	32009	10153	8548	11159	42033
Ce	21225	19490	20837	18280	20596	24357	15226	16156	16665	68595	23280	17080	22497	67435
Pr	2273	2002	2192	1877	2142	2484	1527	1693	1707	7216	2441	1786	2326	6240
Nd	8054	7245	7803	6528	7566	8635	5367	5930	6009	25474	8284	6314	7930	20858
Sm	832	731	823	709	792	856	562	596	626	2461	792	639	765	1976
Eu	164	149	165	148	163	181	128	124	138	479	160	135	162	478
Gd	314	343	321	280	306	347	251	238	261	959	292	261	307	883
Tb	26.0	22.3	27.2	24.3	26.2	27.5	21.4	19.1	21.8	70.9	22.2	21.4	26.4	66.4
Dy	82.8	73.6	87.5	79.0	85.4	91.6	76.2	62.9	73.4	220	70.9	70.9	91.7	225
Ho	9.08	7.87	9.73	8.90	9.61	10.2	9.23	6.91	8.28	22.9	7.80	7.97	10.6	24.6
Er	13.3	11.7	14.1	13.0	14.2	14.7	14.6	9.74	11.9	30.8	10.4	11.3	16.3	33.5
Tm	0.97	0.86	1.05	1.00	1.07	1.14	1.26	0.75	0.93	2.15	0.81	0.87	1.32	2.07
Yb	3.92	3.70	4.19	4.07	4.55	4.77	5.59	3.05	3.84	8.26	3.25	3.61	5.63	7.25
Lu	0.34	0.30	0.37	0.35	0.40	0.40	0.52	0.26	0.33	0.69	0.27	0.31	0.50	0.57
Y	139	127	151	140	149	166	183	110	135	352	115	126	205	440

and d). Both ages are identical, within error, to the recommended values of 356.5 ± 1.0 and 463 Ma, respectively, which indicates that our analytical technique is reliable and the matrix effect is insignificant, since the 91500 zircon standard was used as the internal standard in this study. For Sr isotope determination, 32 analyses were conducted of the IR standard and yield $^{87}Rb/^{87}Sr$ and $^{87}Sr/^{86}Sr$ ratios of 0.00018 ± 1 and 0.70293 ± 2, respectively (Fig. 3e). However, for the TAZ standard, *in situ* Sr isotopic analyses could not be determined, due to its low concentration of Sr (48 ppm). In terms of Nd isotopes, nineteen analyses for IR perovskite yield $^{147}Sm/^{144}Nd$ and $^{143}Nd/^{144}Nd$ ratios of 0.0888 ± 17 and 0.522615 ± 9 (Fig. 3f), respectively, whereas twenty analyses of TAZ perovskite yield respective values of 0.0987 ± 3 and 0.522508 ± 8 (Fig. 3f).

4. Analytical results

4.1. Chemical composition of Perovskite

In this study, twenty-one kimberlite whole-rock samples without visible crustal fragments were selected for perovskite separation and geochemical analyses. Eight samples were devoid of perovskite, but contained abundant titanite. The remaining 13 samples contained enough perovskite for further study. In addition, perovskite separated from the residual heavy mineral fraction, after diamond extraction at the Mengyin mine, was also selected for analysis (MY6). Petrographic and pseudocolour imaging indicate that most of the perovskite is enclosed within ilmenite (Fig. 2e and f), and may contain titanite inclusions (Fig. 2h). Five of them (MY20, MY21, MY27, MY31 and MY32) display pockmarked internal structure as shown in Fig. 2g–o. Major element analyses indicate that these pockmarked perovskites have lower CaO concentrations than the others, indicating alteration after crystallization.

The major and trace element data for perovskites are listed in Table 2 and the REE patterns are shown in Fig. 4. It is noted that the major elements usually total less than 100% since REEs are abundant but are not measured by microprobe. From the data, the unaltered perovskites show similar chemical compositions to other kimberlites from around the world (Chakhmouradian and Mitchell, 2000, 2001), but the altered perovskites contain higher SiO_2 but with less CaO than the unaltered ones (Table 2). All these perovskites contain high Sr, Nb, Ta, Zr, Hf and REE, with minor Rb concentrations, but the altered perovskites contain much less Sr; 503–1145 ppm compared to 1284–2467 ppm for the unaltered ones. However, the altered perovskites have relatively higher REE concentrations than the unaltered ones (see below). As is typical in other areas of the world (Mitchell and Reed, 1988; Melluso et al., 2008), the Mengyin perovskites show highly fractionated REE, with La/Yb ratios of 1448–5798, which is much higher than those of the host kimberlite (73–539) (Fig. 4).

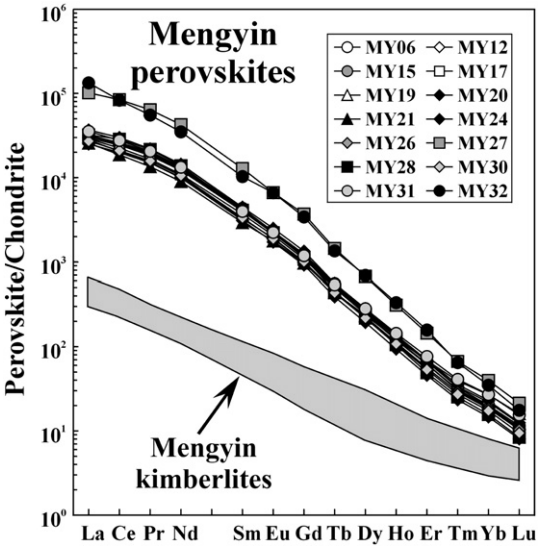

Fig. 4. REE patterns of the perovskites from the Mengyin kimberlites. Field of whole-rock data for the Mengyin kimberlites is from Dong (1994) and Chi and Lu (1996).

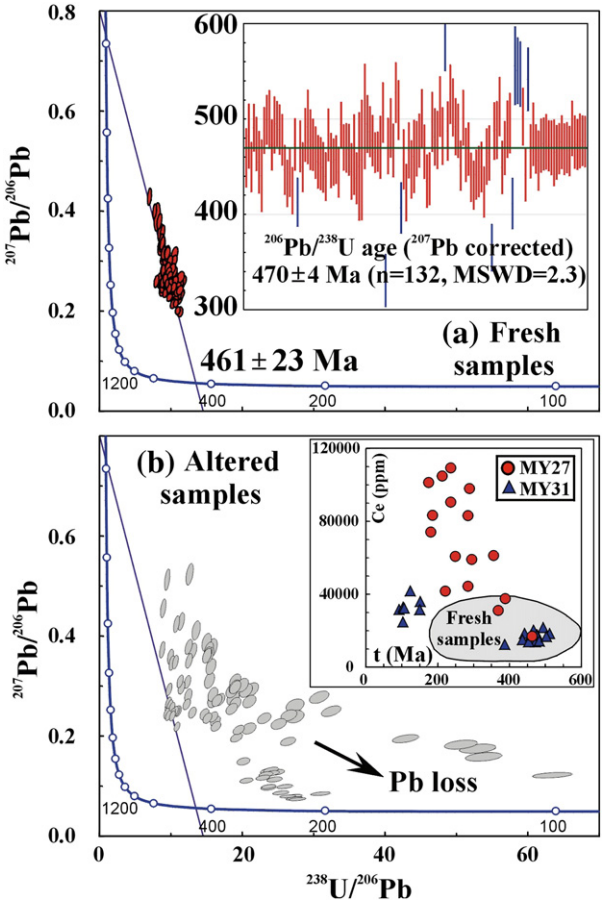

Fig. 5. ICP–MS U–Pb geochronological data for perovskites from the Mengyin kimberlites, Shandong Province, China. (a) fresh perovskites; (b) altered perovskites.

4.2. Perovskite U–Pb isotopic ages

Fourteen samples of perovskite have been analyzed for U–Pb age determination, and the complete data set is given in the supplementary table. They have high U and Th concentrations (Table 2), making them suitable for U–Pb isotopic dating. However, the high Pb concentration means that correction for common lead is necessary. On the Tera–Wasserburg Concordia diagram (Fig. 5), the nine fresh perovskites have an intercept age of 461 ± 23 Ma. If the ^{207}Pb correction method is applied, the $^{206}Pb/^{238}U$ weighted mean age is 470 ± 4 Ma (Fig. 5a). However, the altered perovskites are normally higher in REEs and show a large variation of U–Pb isotopes (Fig. 5b), indicating Pb loss, possibly during the Mesozoic.

4.3. Sr–Nd–Hf isotopes

The whole-rock kimberlitic samples (Tables 3–5) show considerable variation in Sr–Nd–Hf isotopic composition. The rocks have more Sr (82–1148 ppm) than Rb (1.8–160 ppm) with Rb/Sr ratios of 0.02–0.41 (Fig. 6a), whereas the perovskites tend to contain more Sr (234–3819) and even less Rb (1.5–22.2 ppm), with Rb/Sr ratios of 0.0005–0.008 (Fig. 6a). However, it was found that the results obtained by the ID–TIMS method are different from those obtained

Table 3
Rb-Sr isotopic composition of the Mengyin kimberlites and perovskites.

Sample	Analysis	Sample (mg)	Rb (ppm)	Sr (ppm)	$^{87}Rb/^{86}Sr$	$^{87}Sr/^{86}Sr$	$2\sigma_m$	$(^{87}Sr/^{86}Sr)_i$
MY06	Pv (ID)	4.3	15.7	2876	0.0158	0.703849	13	0.7037
MY06	Pv (laser)				0.0018	0.703673	31	0.7036
MY12	WR (ID)	102	113	364	0.9021	0.710838	21	0.7048
MY12	Pv (ID)	8.2	2.08	3818	0.0016	0.703667	11	0.7037
MY12(Re)	Pv (ID)	7.3	2.08	3819	0.0016	0.703644	20	0.7036
MY12	Pv (laser)				0.0007	0.703652	15	0.7036
MY13	WR (ID)	130	131	579	0.6536	0.710390	10	0.7060
MY14	WR (ID)	125	93.0	920	0.2924	0.706624	11	0.7047
MY15	WR (ID)	104	88.5	826	0.3098	0.706100	15	0.7040
MY15 (Re)	WR (ID)	123	86.0	831	0.2995	0.706044	13	0.7040
MY15	Pv (ID)	6.9	14.6	3263	0.0129	0.703845	15	0.7038
MY15	Pv (laser)				0.0023	0.703737	33	0.7037
MY16	WR (ID)	123	46.1	570	0.2340	0.706628	12	0.7051
MY17	WR (ID)	132	113	593	0.5496	0.707962	11	0.7043
MY17 (Re)	WR (ID)	130	110	598	0.5344	0.707909	14	0.7043
MY17	Pv (ID)	5.2	5.78	2057	0.0081	0.703968	14	0.7039
MY17	Pv (laser)				0.0039	0.703786	73	0.7038
MY18	WR (ID)	96	46.9	537	0.2531	0.706827	14	0.7051
MY19	WR (ID)	125	160	1148	0.4035	0.706919	13	0.7042
MY19	Pv (ID)	4.7	22.2	2760	0.0232	0.704302	13	0.7041
MY19	Pv (laser)				0.0023	0.703814	42	0.7038
MY20	WR (ID)	123	107	259	1.1967	0.713599	13	0.7056
MY20	Pv (laser)				0.0028	0.703820	150	0.7038
MY21	WR (ID)	97	7.6	182	0.1208	0.705752	14	0.7049
MY22	WR (ID)	121	22.6	147	0.4438	0.708732	12	0.7058
MY23	WR (ID)	113	20.4	152	0.3876	0.708205	14	0.7056
MY24	WR (ID)	127	38.7	436	0.2572	0.706059	13	0.7043
MY24	Pv (ID)	4.1	5.5	1813	0.0087	0.704276	24	0.7042
MY24	Pv (laser)				0.0003	0.703644	88	0.7036
MY25	WR (ID)	118	54.1	595	0.2627	0.706191	15	0.7044
MY26	WR (ID)	132	27.3	487	0.1622	0.705383	14	0.7043
MY26	Pv (laser)				0.0006	0.703800	49	0.7038
MY27	WR (ID)	98	24.0	539	0.1289	0.705431	30	0.7046
MY27	Pv (laser)				0.0040	0.703691	66	0.7037
MY28	WR (ID)	95	10.9	370	0.0850	0.705834	12	0.7053
MY28	Pv (ID)	3.8	4.7	1826	0.0074	0.703812	12	0.7038
MY28 (Re)	Pv (ID)	4.5	4.4	1806	0.0071	0.703829	10	0.7038
MY28	Pv (laser)				0.0003	0.703674	75	0.7037
MY29	WR (ID)	130	17.1	173	0.2859	0.706999	11	0.7051
MY30	WR (ID)	114	11.5	369	0.0901	0.705444	13	0.7048
MY30	Pv (laser)				0.0011	0.703714	85	0.7037
MY31	WR (ID)	93	1.8	82	0.0639	0.706251	14	0.7058
MY31	Pv (laser)				0.0007	0.703740	76	0.7037
MY32	WR (ID)	96	22.4	244	0.2655	0.706651	11	0.7049

WR: whole-rock, Pv: perovskite, ID: isotopic dilution, Re: replicate.

by laser ablation. For ID–TIMS analyses, the Rb and Sr concentrations are 2.1–22.2 and 672–3819 ppm, respectively; whereas the results by laser ablation are 0.44–3.81 and 503–2467 ppm, both lower than the ID–TIMS values. We propose that some later fluid(s) may have enriched Rb and Sr along the mineral cleavages, thus affecting the whole-mineral analyses but not being evident in the laser ablation analyses, since such sites were avoided. Alternatively, some heterogeneity might exist among the different mineral grains, although this would not be expected to produce such a systematic variation in the results. The whole-rock samples yield an "errorchron" with a reference age of ~500 Ma (Fig. 6b), with an initial Sr isotopic ratio of 0.705 ± 3. The perovskites show lower initial Sr ratios than the whole-rocks (Fig. 6b); 0.7036–0.7042 by TIMS and 0.7036–0.7038 by laser ablation (Fig. 7a).

The whole-rock samples have Sm and Nd concentrations of 6.7–10.9 and 52–94 ppm, with Sm/Nd ratios ranging from 0.112–0.131, whereas the perovskites have Sm and Nd concentrations of 402–595 and 3730–5508 ppm with Sm/Nd ratios ranging from 0.103–0.113 (Fig. 6c). The ID–TIMS analyses on perovskites give Sm and Nd concentrations of 132–595 and 1378–5508 ppm, whereas those by laser ablation are 562–1976 and 5367–20858 ppm; much higher than the former. The $^{147}Sm/^{144}Nd$ and $^{143}Nd/^{144}Nd$ ratios of whole-rocks are 0.068–0.078 and 0.512167–0.512267 (Fig. 6d), respectively, with $\varepsilon_{Nd}(t)$ values of −2.0 to +0.26, whereas the perovskites analysed by ID–TIMS give $^{147}Sm/^{144}Nd$, $^{143}Nd/^{144}Nd$ and $\varepsilon_{Nd}(t)$ values of 0.062–0.069, 0.512209–0.512247 (Fig. 6d), and −0.36 to +0.30, respectively; thus showing much less variation than the whole-rock samples. The perovskites analyzed by laser ablation give $^{147}Sm/^{144}Nd$, $^{143}Nd/^{144}Nd$ and $\varepsilon_{Nd}(t)$ values of 0.063–0.069, 0.512219–0.512305 and −0.24 to +1.66, slightly higher than those obtained by ID–TIMS for both whole-rocks and perovskites (Fig. 6b).

The whole-rock samples contained 0.018–0.064 ppm Lu and 2.92–5.05 ppm Hf with Lu/Hf ratios of ~0.01 (0.007–0.020, Fig. 6e), whereas the perovskites contain much more Lu (0.267–0.520 ppm) and Hf (49.7–147.2 ppm), with Lu/Hf ratios of 0.0023–0.0061 (Fig. 6e). The perovskites show lower $^{176}Lu/^{177}Hf$ and a narrower range of $^{176}Hf/^{177}Hf$ ratios compared to the whole-rock samples (Fig. 6f). The obtained $\varepsilon_{Hf}(t)$ values range from +0.52 to −6.13, showing some variation.

5. Discussion

5.1. Emplacement age of the Mengyin kimberlite

Perovskite normally has high U concentrations, which makes this mineral an excellent candidate to date kimberlite using the U–Pb isotopic method (Kramers and Smith, 1983; Smith et al., 1989, 1994; Kinny et al., 1997; Heaman et al., 2003, 2004; Cox and Wilton, 2006; Batumike et al., 2008). For the Mengyin kimberlite, it has previously been established that U–Pb dating of perovskite by the SHRIMP

Table 4
Sm-Nd isotopic composition of the Mengyin kimberlites and perovskites.

Sample	Analysis	Sample (mg)	Sm (ppm)	Nd (ppm)	$^{147}Sm/^{144}Nd$	$^{143}Nd/^{144}Nd$	$2\sigma_m$	$\varepsilon_{Nd}(t)$	T_{DM} (Ma)
MY06	Pv (ID)	4.3	595	5508	0.0653	0.512234	12	0.02	941
MY06	Pv (laser)				0.0641	0.512219	12	−0.21	949
MY12	WR (ID)	102	8.5	70	0.0730	0.512231	13	−0.52	996
MY12	Pv (ID)	8.2	520	4586	0.0686	0.512225	12	−0.36	971
MY12(Re)	Pv (ID)	7.3	530	4765	0.0673	0.512235	14	−0.10	953
MY12	Pv (laser)				0.0664	0.512229	12	−0.16	954
MY13	WR (ID)	130	7.5	57	0.0790	0.512048	9	−4.45	1246
MY13 (Re)	WR (ID)		7.0	53	0.0795	0.512044	9	−4.55	1255
MY14	WR (ID)	125	7.7	59	0.0792	0.512225	11	−0.99	1047
MY15	WR (ID)	104	8.4	66	0.0771	0.512167	12	−2.00	1096
MY15 (Re)	WR (ID)	123	8.5	67	0.0768	0.512170	12	−1.93	1090
MY15	Pv (ID)	6.9	440	3994	0.0666	0.512230	10	−0.15	953
MY15	Pv (laser)				0.0640	0.512226	7	−0.07	941
MY16	WR (ID)	123	8.1	69	0.0711	0.512238	10	−0.26	975
MY17	WR (ID)	132	9.4	78	0.0724	0.512197	12	−1.15	1028
MY17 (Re)	WR (ID)	130	9.3	78	0.0725	0.512203	13	−1.03	1022
MY17	Pv (ID)	5.2	469	4203	0.0675	0.512242	13	0.04	946
MY17	Pv (laser)				0.0687	0.512215	19	0.37	983
MY18	WR (ID)	96	8.3	69	0.0729	0.512206	11	−0.98	1021
MY19	WR (ID)	125	7.2	59	0.0740	0.512200	12	−1.18	1036
MY19	Pv (ID)	4.7	402	3730	0.0651	0.512235	8	0.04	939
MY19	Pv (laser)				0.0649	0.512220	9	−0.24	952
MY20	WR (ID)	123	9.3	79	0.0710	0.512250	14	−0.02	961
MY20	Pv (laser)				0.0670	0.512234	15	−0.09	952
MY21	WR (ID)	97	9.1	78	0.0705	0.512253	13	0.07	955
MY21	Pv (laser)				0.0671	0.512272	22	0.64	913
MY22	WR (ID)	121	9.2	75	0.0743	0.512262	14	0.01	971
MY22	Pv (ID)	5.2	337	3238	0.0629	0.512214	11	−0.24	947
MY23	WR (ID)	113	8.4	65	0.0777	0.512242	12	−0.58	1017
MY24	WR (ID)	127	9.0	76	0.0712	0.512243	13	−0.16	970
MY24	Pv (ID)	4.1	500	4681	0.0646	0.512247	13	0.30	923
MY24	Pv (laser)				0.0661	0.512269	6	0.65	910
MY25	WR (ID)	118	8.1	72	0.0681	0.512211	10	−0.60	983
MY26	WR (ID)	132	7.7	65	0.0715	0.512243	14	−0.19	972
MY26	Pv (laser)				0.0691	0.512281	10	0.70	916
MY27	WR (ID)	98	7.9	71	0.0675	0.512251	12	0.21	937
MY27	Pv (laser)				0.0642	0.512236	10	0.11	932
MY28	WR (ID)	95	9.9	86	0.0693	0.512259	14	0.26	941
MY28	Pv (ID)	3.8	553	5390	0.0620	0.512225	12	0.03	930
MY28 (Re)	Pv (ID)	4.5	550	5338	0.0623	0.512209	11	−0.30	948
MY28	Pv (laser)				0.0640	0.512224	8	−0.10	943
MY29	WR (ID)	130	6.7	52	0.0769	0.512259	13	−0.20	993
MY30	WR (ID)	114	7.9	66	0.0718	0.512256	14	0.05	960
MY30	Pv (laser)				0.0697	0.512254	9	0.13	949
MY31	WR (ID)	93	10.9	94	0.0701	0.512246	14	−0.04	959
MY31	Pv (laser)				0.0701	0.512247	12	−0.02	958
MY32	WR (ID)	96	7.6	62	0.0744	0.512267	13	0.11	966
MY32	Pv (laser)				0.0625	0.512290	12	1.27	867

WR: whole-rock, Pv: perovskite, ID: isotopic dilution, Re: replicate.
The notation of $\varepsilon_{Nd}(t)$ and T_{DM} are defined as:

$$\varepsilon_{Nd}(t) = \left(\left(^{143}Nd/^{144}Nd\right)_S - \left(^{147}Sm/^{144}Nd\right)_S \times \left(e^{\lambda t} - 1\right)\right) / \left(\left(^{143}Nd/^{144}Nd\right)_{CHUR} - \left(^{147}Sm/^{144}Nd\right)_{CHUR} \times \left(e^{\lambda t} - 1\right)\right) - 1) \times 10000$$

$$T_{DM} = 1/\lambda \times \ln\left\{1 + \left[\left(^{143}Nd/^{144}Nd\right)_S - 0.51315\right] / \left[\left(^{147}Sm/^{144}Nd\right)_S - 0.2137\right]\right\}$$

where s = sample, and $(^{143}Nd/^{144}Nd)_{CHUR} = 0.512638$, and $(^{147}Sm/^{144}Nd)_{CHUR} = 0.1967$. The decay constant ($\lambda$) used in calculations was 0.654×10^{-11}/y for ^{147}Sm. $t = 470$ Ma.

technique yielded an age of 456 ± 8 Ma, although no analytical details were reported (cited by Dobbs et al. (1994)). Furthermore, Rb–Sr isotopic analyses of phlogopite yield an isochron age of 475 ± 3 Ma (Dobbs et al., 1994), and the Ar–Ar age of the same mineral is 465 ± 3 Ma (Zhang and Yang, 2007). In this study, nine fresh samples yield U–Pb ages of 466 ± 16 (MY6), 467 ± 9 (MY12), 466 ± 15 (MY15), 451 ± 11 (MY17), 475 ± 9 (MY19), 467 ± 15 (MY24), 471 ± 14 (MY27), 479 ± 19 (MY28) and 472 ± 5 (MY30) Ma, respectively (Table 6). If these ages are calculated together, the obtained weighted age is 471 ± 3 Ma ($n = 9$, MSWD = 0.5), which is identical to the weighted mean age of 470 ± 4 Ma from 132 individual analyses from the above 9 fresh samples (Fig. 5a). Considering that our analyses were undertaken on a suite of samples, the age of 470 ± 4 Ma is considered as the best estimate for the emplacement of the Mengyin kimberlite.

However, amongst our dated samples, 5 out of 14 show large age variations, and are mostly discordant and younger than ~470 Ma (Fig. 5b). Detailed imaging indicates that these perovskites are mostly altered (Fig. 2g–o), suggesting that alteration can reset the U–Pb isotopic system of perovskites; contrary to what was previously thought, i.e. that the mineral is highly resistant to weathering and alteration (Heaman, 1989). A similar result was obtained from the Elwin Bay kimberlite on Somerset Island, Canada, where fresh perovskites record a U–Pb age of 113 ± 6 Ma (Wu et al., 2009), markedly different from the younger ages of 27–36 Ma obtained by Smith et al. (1989). Subsequently it was verified by petrography that perovskite is unstable in CO_2-rich environments, such as kimberlite (Mitchell and Chakhmouradian, 1998; Chakhmouradian and Mitchell, 2000). In sample MY31 of this study, thirteen analyses of the fresh grains yield a U–Pb age of

Table 5
Lu–Hf isotope composition of the Mengyin kimberlites and perovskites (by isotopic dilution).

Sample	Analysis	Sample (mg)	Lu (ppm)	Hf (ppm)	$^{176}Lu/^{177}Hf$	$^{176}Hf/^{177}Hf$	2σ	$\varepsilon_{Hf}(t)$	T_{DM} (Ma)
MY06	Pv	4.3	0.389	109	0.0005	0.282426	10	−2.05	1152
MY12	WR	102	0.049	3.80	0.0018	0.282424	9	−2.52	1196
MY12	Pv	8.2	0.338	147	0.0003	0.282436	5	−1.64	1133
MY13	WR	130	0.056	3.86	0.0021	0.282168	6	−11.68	1572
MY13 (Re)	WR	124	0.049	3.57	0.0019	0.282174	13	−11.41	1558
MY14	WR	125	0.037	4.32	0.0012	0.282447	5	−1.52	1144
MY15	WR	104	0.064	3.97	0.0023	0.282294	8	−7.29	1400
MY15 (Re)	WR	123	0.064	3.97	0.0023	0.282297	7	−7.16	1395
MY15	Pv	6.9	0.366	145	0.0004	0.282309	5	−6.13	1308
MY15 (Re)	Pv	4.8	0.343	169	0.0003	0.282337	8	−5.11	1267
MY16	WR	123	0.018	3.79	0.0007	0.282473	6	−0.45	1093
MY17	WR	132	0.050	4.42	0.0016	0.282401	10	−3.27	1222
MY17 (Re)	WR	130	0.051	4.44	0.0016	0.282396	5	−3.47	1231
MY17	Pv	5.2	0.520	142	0.0005	0.282325	38	−5.64	1293
MY18	WR	98	0.062	3.82	0.0023	0.282374	5	−4.45	1284
MY19	WR	125	0.058	2.92	0.0028	0.282436	8	−2.40	1210
MY19	Pv	4.7	0.283	57.9	0.0007	0.282419	10	−2.36	1168
MY20	WR	123	0.046	4.34	0.0015	0.282435	6	−2.05	1171
MY20	Pv	4.3	0.308	87.5	0.0005	0.282449	14	−1.24	1121
MY21	WR	97	0.046	3.93	0.0016	0.282488	8	−0.22	1099
MY22	WR	121	0.044	3.38	0.0019	0.282480	6	−0.56	1117
MY22	Pv	5.3	0.302	32.3	0.0013	0.282437	50	−1.90	1161
MY23	WR	113	0.038	3.25	0.0017	0.282467	9	−0.94	1129
MY23	Pv	3.8	0.302	49.7	0.0009	0.282465	31	−0.79	1109
MY24	WR	127	0.032	3.70	0.0012	0.282485	9	−0.17	1090
MY24	Pv	4.1	0.267	82.0	0.0005	0.282484	7	0.00	1071
MY25	WR	118	0.050	4.21	0.0017	0.282443	4	−1.81	1164
MY26	WR	132	0.041	4.07	0.0014	0.282446	6	−1.63	1152
MY27	WR	98	0.028	3.98	0.0010	0.282490	9	0.06	1077
MY28	WR	95	0.043	5.05	0.0012	0.282485	6	−0.18	1091
MY28	Pv	3.8	0.271	76.3	0.0005	0.282483	10	−0.03	1073
MY28 (Re)	Pv	4.5	0.284	76.4	0.0005	0.282499	14	0.52	1052
MY29	WR	130	0.028	3.39	0.0012	0.282465	6	−0.87	1117
MY30	WR	114	0.035	3.74	0.0013	0.282469	9	−0.77	1117
MY31	WR	93	0.048	4.17	0.0017	0.282479	6	−0.54	1113
MY32	WR	96	0.037	4.13	0.0013	0.282469	8	−0.75	1115

WR: whole-rock, Pv: perovskite, Re: replicate.
The notations of $\varepsilon_{Hf}(t)$ and T_{Hf} defined as:

$$\varepsilon_{Hf(t)} = \left(\left(^{176}Hf/^{177}Hf\right)_S - \left(^{176}Lu/^{177}Hf\right)_S \times \left(e^{\lambda t} - 1\right)\right) / \left(\left(^{176}Hf/^{177}Hf\right)_{CHUR} - \left(^{176}Lu/^{177}Hf\right)_{CHUR} \times \left(e^{\lambda t} - 1\right)\right) - 1) \times 10000$$

$$T_{Hf} = 1/\lambda \times \left(1 + \left(\left(^{176}Hf/^{177}Hf\right)_S - \left(^{176}Hf/^{177}Hf\right)_{DM}\right) / \left(\left(^{176}Lu/^{177}Hf\right)_S - \left(^{176}Lu/^{177}Hf\right)_{DM}\right)\right)$$

where, $(^{176}Lu/^{177}Hf)_S$ and $(^{176}Hf/^{177}Hf)_S$ are the measured values of samples, $(^{176}Lu/^{177}Hf)_{CHUR} = 0.0332$ and $(^{176}Hf/^{177}Hf)_{CHUR} = 0.282772$ (Blichert-Toft and Albarede, 1997); $(^{176}Lu/^{177}Hf)_{DM} = 0.0384$ and $(^{176}Hf/^{177}Hf)_{DM} = 0.28325$ (Griffin et al., 2000), The decay constant (λ) used in calculations was 1.867×10^{-11}/y for ^{176}Lu (Soderlund et al., 2004)), $t = 470$ Ma.

471 ± 14 Ma (Table 6), but seven altered grains yield Mesozoic ages. According to our observations, the perovskites with younger ages show significant replacement by calcite and titanite (Fig. 2g–o). It is also noted that most of these grains have much higher REE concentrations (Fig. 5b), which indicate REE-enrichment of perovskite during alteration. In addition, it is likely that perovskites with high REE concentrations are more easily altered. Therefore, it is necessary to make an assessment of alteration for the perovskite before conducting U–Pb analyses in order to obtain precise age data.

Importantly, the alteration did not change the Sr–Nd isotopic compositions of perovskites. As indicated in Table 6, the fresh samples have $^{87}Sr/^{86}Sr$ ratios ranging from 0.703644 ± 88 to 0.703814 ± 42; whereas the altered samples range from 0.703691 ± 66 to 0.70382 ± 15. However, alteration can decrease Sr concentrations, making it impossible to get high precision using the *in situ* technique. In terms of Nd isotopes, the $^{143}Nd/^{144}Nd$ ratios of the fresh samples range from 0.512207 ± 15 to 0.512281 ± 10, and those of altered samples range between 0.512234 ± 15 and 0.512290 ± 12. The reason for lack of any detectable Sr–Nd isotopic variation between fresh and altered perovskites might be that the mineral contains high Sr and Nd concentrations, which makes it insensitive to the any later addition.

5.2. Obtaining meaningful initial isotopic compositions for kimberlite

Isotopic data are vital in deciphering the petrogenesis of kimberlites. A common procedure is to obtain isotopic ratios from whole-rock material (e.g., Becker and Le Roex, 2006), since it has been suggested that the high incompatible element concentrations and rapid transportation *en route* mean that the effect of contamination by crustal material is minimal (Smith, 1983). However, this conclusion is not supported by leaching experiments, which indicate that there is commonly a crustal isotopic component present (Alibert and Albarede, 1988). Likewise, although it has been argued that, by applying geochemical criteria, whole-rocks without any contamination can be selected (Le Roex et al., 2003) or that a rock can be cleaned to exclude later alteration (Becker and Le Roex, 2006), the contaminant is mostly invisible and cannot be removed. Clearly, the best way to obtain the primary isotopic signature of kimberlite is to analyze perovskite that directly crystallized from the initial magma and remained unaffected by subsequent petrogenetic or weathering processes (Heaman, 1989; Paton et al., 2007a).

As shown in Figs. 6 and 7, whole-rocks from the Mengyin kimberlite show a large variation in Sr–Nd–Hf isotopic composition, indicating that it is impossible to get reliable initial isotopic data from

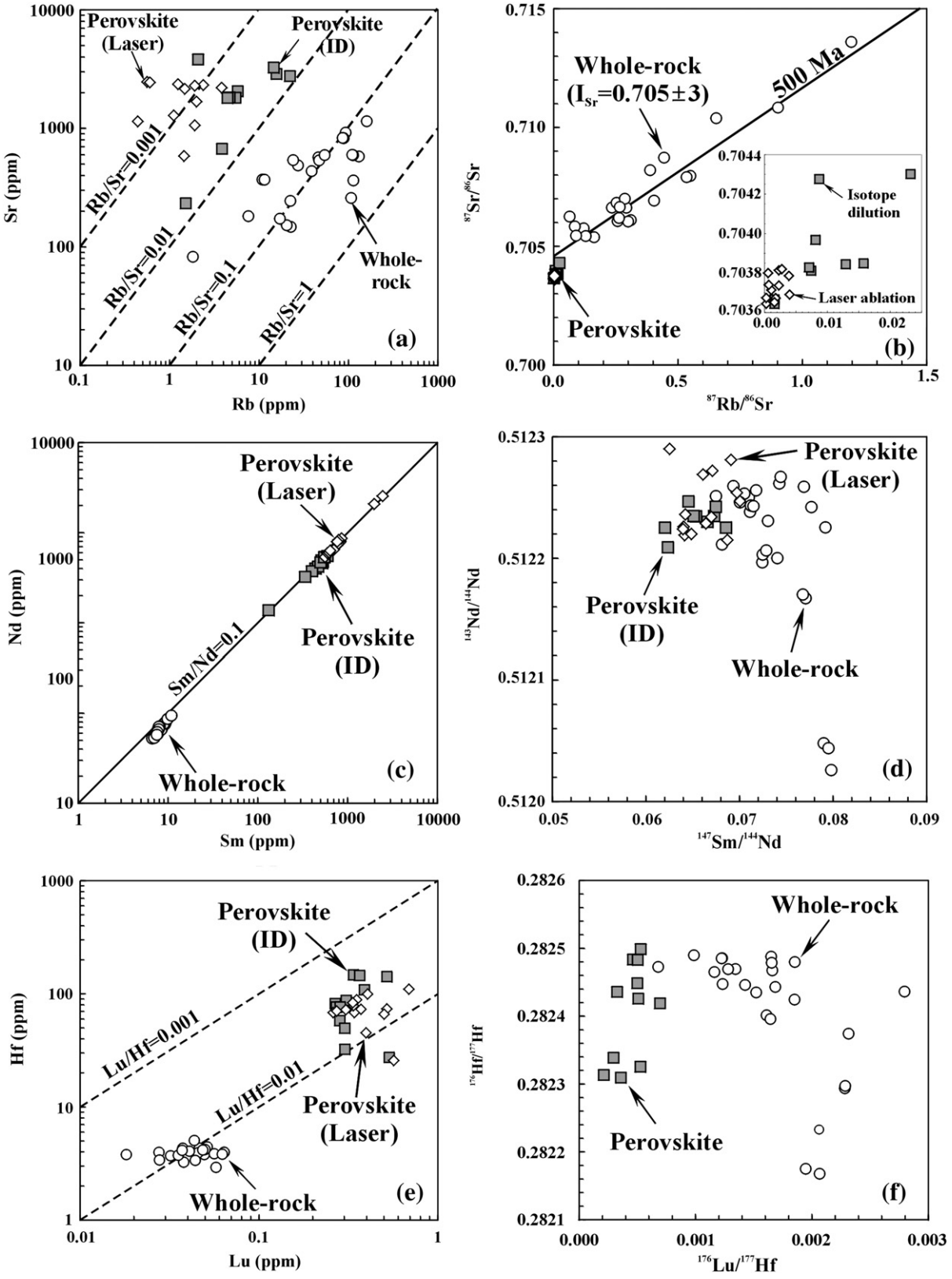

Fig. 6. Sr–Nd–Hf isotopic characterization of Mengyin whole-rock kimberlite and perovskite grains by isotopic dilution TIMS and laser ablation techniques.

whole-rock analyses, even when the samples show no visible sign of crustal and/or mantle contamination. However, the perovskites from these samples have uniform Sr–Nd–Hf isotopic values. Considering that perovskite formed early during kimberlite crystallization and has high Sr, Nd and Hf concentrations, it is reasonable to conclude that analyses of perovskite can provided more reliable initial isotopic compositions of the kimberlitic magma. However, our perovskite analyses indicate that the ID–TIMS method records higher $^{87}Rb/^{86}Sr$ and $^{87}Sr/^{86}Sr$ ratios than those obtained by laser ablation, although the variation is limited (Fig. 6b). In terms of Nd isotopes, 9 analyses by

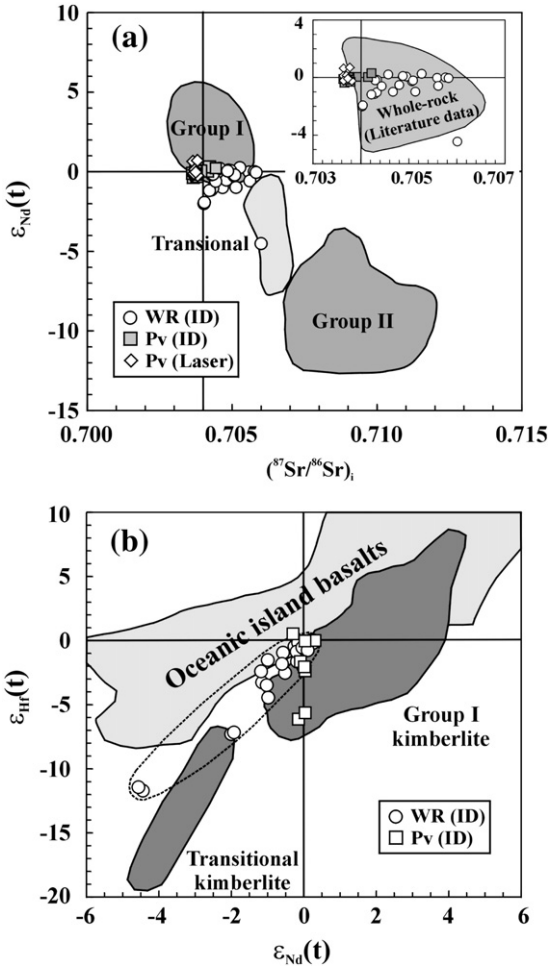

Fig. 7. Genetic discrimination diagrams for the Mengyin kimberlites. (a) $\varepsilon_{Nd}(t)$ vs. $(^{87}Sr/^{86}Sr)_i$, the fields of Group I, II and transitional kimberlites are from the following references (Smith, 1983; Fraser et al., 1985; Heaman, 1989; Nowell et al., 2004; Becker and Le Roex, 2006, Becker et al., 2007). The literature whole-rock Sr–Nd isotopic data in the inset for the Mengyin kimberlites are from Chi and Lu (1996), Luo et al. (1999), and Zhang and Yang (2007). (b) $\varepsilon_{Hf}(t)$ vs. $\varepsilon_{Nd}(t)$ plot, the fields of oceanic island basalts and Group 1 and transitional kimberlites are from Nowell et al. (2004). WR (ID) — whole rock data by ID–TIMS, Pv (ID) — perovskite data by ID–TIMS, and Pv (laser) — *in situ* perovskite analyses by LA–ICPMS.

the ID–TIMS method yield a weighted $\varepsilon_{Nd}(t)$ value of -0.05 ± 0.15 (2σ), whereas a weighted $\varepsilon_{Nd}(t)$ value of 0.13 ± 0.22 (2σ) is obtained from 14 samples by laser ablation analysis; slightly higher although they overlap within errors. This difference is interpreted to result from the passage of enriched fluid along mineral cleavages, since the ID–TIMS data were obtained from bulk analyses of multi-grains, whereas the laser ablation data were obtained on carefully selected minerals without any cleavages or fractures. Although we cleaned the minerals prior to analysis using low concentrations of HCl, it is impossible to drive away all fluid from within the mineral structure. Because of this, laser ablation of perovskite can effectively provide reliable Sr and Nd isotopic compositions, enabling evaluation of the mantle source and petrogenesis of the host kimberlite. Although the Mengyin perovskites have extremely low $^{176}Lu/^{177}Hf$ ratios (commonly <0.001), it is impossible, however, to get precise Hf data by laser ablation, since their Hf concentrations of 45–89 ppm are too low.

5.3. Sr–Nd–Hf isotopic constraints on petrogenesis of the Mengyin kimberlites

According to whole-rock data (Chi and Lu, 1996; Luo et al., 1999; Zhang and Yang, 2007; and this study — Table 3), the Mengyin kimberlite has an initial Sr isotopic ratio between 0.7039 and 0.7065 (Fig. 8a). This value is much higher than those we obtained from perovskite by using either the laser ablation or solution techniques (Fig. 8b). Furthermore, our laser ablation analyses of eleven different samples indicate that the Mengyin kimberlitic perovskites have uniform $^{87}Sr/^{86}Sr$ ratios of 0.70371 ± 12 (2SD) (Fig. 8b), slightly lower than the primitive mantle value of ~0.7040 in the Paleozoic. Considering that these perovskites are believed to have crystallized at an early magmatic stage, we interpret that 0.7037 is the initial $^{87}Sr/^{86}Sr$ ratio of the Mengyin kimberlitic magma.

The whole-rocks have mean $\varepsilon_{Nd}(t)$ values of −2.0 to +0.26 (Figs. 7a and 8c), in contrast to perovskites that have mean $\varepsilon_{Nd}(t)$ values of −0.36 to +1.66 (Fig. 7a and b). For laser ablated perovskites, 14 analyses yield an average value of 0.13 ± 0.22 (Fig. 8d). It is also noted from Fig. 6d that mixing of two members can be used to explain the Nd isotopic variations of the whole-rock samples. One end-member is more radiogenic with $^{143}Nd/^{144}Nd > 0.51226$, but with a lower $^{147}Sm/^{144}Nd$ value, whereas the other end-member is less radiogenic with $^{143}Nd/^{144}Nd < 0.51217$ and $^{147}Sm/^{144}Nd > 0.08$. It is reasonable to conclude that the less radiogenic end-member could be a recycled Archean crustal component, since this is the only kind of crustal material exposed in the area, whereas the radiogenic end-member represents the original kimberlite magma.

The Hf isotopes show similar characteristics to the Nd isotopes, although both whole-rock and perovskite plot beneath the mantle array in the $\varepsilon_{Hf}(t)$ vs. $\varepsilon_{Nd}(t)$ variation diagram (Fig. 7b). This characteristic has also been documented in kimberlites from South Africa and West Greenland (Nowell et al., 2004; Gaffney et al., 2007), from carbonatite and alkaline igneous rocks (Janney et al., 2002; Bizimis et al., 2003), and HIMU-type basalts (Salters and White, 1998). Salters and White (1998) first proposed that this phenomenon is related to recycling of oceanic crust. Alternatively, Griffin et al. (2000) attributed this to derivation in the SCLM. However, it is now demonstrated that the SCLM will have positive $\varepsilon_{Hf}(t)$ values, and should locate above the $\varepsilon_{Hf}(t)-\varepsilon_{Nd}(t)$ mantle array (Nowell et al., 2004). Therefore, it was again proposed that this component is ancient oceanic crust underplated beneath the lithosphere, but isolated from the convecting mantle in order to retain its distinctive Hf isotopic signature (Nowell et al., 2004; Gaffney et al., 2007).

However, it is difficult to understand why most ocean island basalts (OIB) do not show any such deviation if a special geochemical reservoir exists below the lithosphere. In the Mengyin case, the whole-rock and perovskite data show different trends in the $\varepsilon_{Hf}(t)-\varepsilon_{Nd}(t)$ variation diagram (Fig. 7b). Most whole-rock samples plot near to the Group I kimberlites, but two samples with more negative $\varepsilon_{Nd}(t)$ and $\varepsilon_{Hf}(t)$ values are close to the field of

Table 6
Summary of U-Pb age and Sr-Nd isotopes of the perovskites from the Mengyin kimberlite.

Sample	U–Pb age (Ma)[a]	$^{87}Rb/^{86}Sr$	$^{87}Sr/^{86}Sr$	$^{147}Sm/^{144}Nd$	$^{143}Nd/^{144}Nd$	ε_{Nd} (470)
Fresh samples						
MY06	466 ± 16	0.0018	0.703673 ± 31	0.0641	0.512219 ± 12	−0.21
MY12	467 ± 09	0.0007	0.703676 ± 11	0.0664	0.512229 ± 12	−0.16
MY15	466 ± 15	0.0023	0.703737 ± 33	0.0640	0.512224 ± 07	−0.07
MY17	451 ± 11	0.0039	0.703786 ± 73	0.0687	0.512207 ± 15	+0.37
MY19	475 ± 09	0.0023	0.703814 ± 42	0.0649	0.512217 ± 06	−0.24
MY24	467 ± 15	0.0003	0.703644 ± 88	0.0661	0.512269 ± 06	+0.65
MY26	471 ± 14	0.0006	0.703800 ± 49	0.0691	0.512281 ± 10	+0.70
MY28	479 ± 19	0.0003	0.703674 ± 75	0.0640	0.512224 ± 08	−0.10
MY30	472 ± 05	0.0011	0.703714 ± 85	0.0697	0.512254 ± 09	+0.13
MY31	471 ± 14	0.0007	0.703740 ± 76	0.0701	0.512247 ± 12	−0.02
Altered samples						
MY20	274 ± 30	0.0028	0.70382 ± 15	0.0670	0.512234 ± 15	−0.09
MY21	286 ± 25			0.0671	0.512272 ± 22	+0.64
MY27	238 ± 25	0.0040	0.703691 ± 66	0.0642	0.512236 ± 10	+0.11
MY32	243 ± 07			0.0625	0.512290 ± 12	+1.27

[a] Only fresh perovskites are included in the U–Pb age calculation.

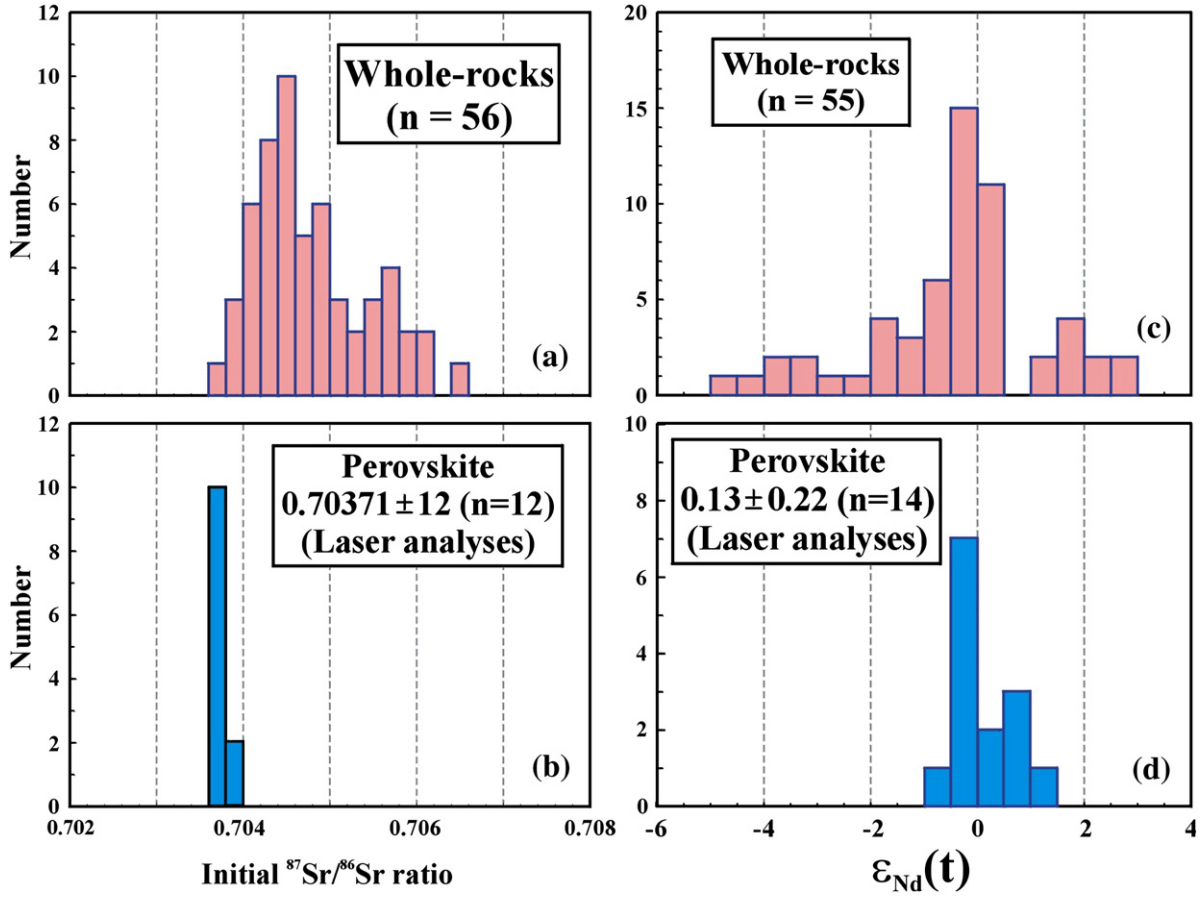

Fig. 8. Histograms comparing the initial Sr–Nd isotopic composition of perovskite with whole-rock values for the Mengyin kimberlites. Data sources are Chi and Lu (1996); Luo et al. (1999); Zhang and Yang (2007) and this study. (a) Whole-rock Sr isotopes; (b) Perovskite Sr isotopes (laser analyses); (c) Whole-rock Nd isotopes, and (d) Perovskite Nd isotopes (laser analyses).

transitional kimberlite (Fig. 7b). These isotopic variations can also be explained by mixing of two components, one primitive and another less radiogenic. The primitive mantle has $\varepsilon_{Nd}(t)$ and $\varepsilon_{Hf}(t)$ values of zero, but the less radiogenic end-member has $\varepsilon_{Nd}(t) < -2$ and $\varepsilon_{Hf}(t) < -7$. Considering that our samples were collected from a single kimberlitic pipe, it is reasonable to conclude that the above isotopic variation was derived from contamination by crustal material, and is not a feature of the mantle source. It is now known that crustal materials are mostly located along the terrestrial array (Vervoort et al., 1999), but a recent discovery indicates that felsic and sedimentary granulites can significantly deviate from the above array and display obvious Nd–Hf isotopic decoupling (Schmitz et al., 2004). As for the perovskites, which should record the primary isotopic composition of the magma, they show identical $\varepsilon_{Nd}(t)$ values, but with some variations in $\varepsilon_{Hf}(t)$. As shown in Fig. 9, perovskites with higher Hf concentrations possess more negative $\varepsilon_{Hf}(t)$ values, but without significant Sr–Nd isotopic variations. This is difficult to explain, but it might be ascribed to the variable effects of crustal contamination. This proposal is supported by differences in the La/Yb ratios between whole-rocks and perovskites, as discussed below. Therefore, if this assumption is correct, Hf–Nd isotopic decoupling of kimberlites could result from crustal contamination and invoking a hidden geochemical reservoir beneath the lithosphere is unnecessary. More work is needed to verify this conclusion.

Overall, the data show that the Mengyin kimberlites should be classified as belonging to Group I (Smith, 1983) and that the primary magma was derived from a weakly depleted or primitive mantle source, characterized by low initial Sr, and high $\varepsilon_{Nd}(t)$ and $\varepsilon_{Hf}(t)$ values (Fig. 7). This kind of primitive source could be either deep asthenospheric or lithospheric mantle. However, it is difficult to believe that ancient lithospheric mantle can avoid late metasomatism which would make it enriched in Sr–Nd–Hf. Therefore, we propose a deep mantle source. If this proposal is correct, the remaining question that needs to be answered is why the kimberlitic magma is highly enriched in incompatible elements. One possibility is that the degree of mantle melting was extremely small, which would result in significant elevation of these elements in the melt. Alternatively, the

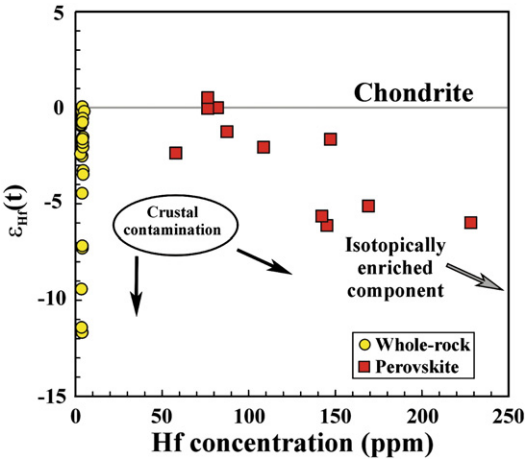

Fig. 9. Hf isotopic variations of perovskites and their host kimberlites. Perovskites with higher Hf concentration display more negative $\varepsilon_{Hf}(t)$ values, indicating contamination from non-radiogenic (ancient crustal) materials.

mantle source may have only just been metasomatised prior to formation of the kimberlitic magma. During emplacement, crustal contamination has significantly modified the kimberlitic magma, even during the very early stages when perovskite crystallized. Therefore, the whole-rock analyses do not represent the composition of the primary magma.

5.4. Tectonic implications

It was recently proposed that the formation of Paleozoic kimberlites in the North China Craton was effected by subduction of oceanic lithosphere (Zhang and Yang, 2007), based on the large variation in initial $^{87}Sr/^{86}Sr$ isotopic compositions of whole-rock samples. It was argued that the rapid eruption of kimberlite prevented any crustal contamination or crystallization during ascent, and that the Sr isotopic variations should be related to the involvement of oceanic water during partial melting of the asthenosphere. However, this argument is not supported by the following lines of evidence. Firstly, the Paleozoic kimberlites are mostly distributed in the eastern part of the NCC (Fig. 1), at Mengyin, Fuxian and Tieling; and there is no available evidence indicating that there was subduction in the area during the early Paleozoic. Secondly, as shown in Fig. 7a, perovskite is a primary mineral that crystallized during the early stage of magma evolution, and shows less chemical variation than the whole-rock samples, indicating that the primary magma was homogeneous in Sr isotopic composition. Thirdly, as shown in Fig. 4, the perovskites have much higher La/Yb ratios than the whole-rocks. One explanation is LREEs are more compatible than HREEs in perovskite, which results in the residual magma having higher La/Yb values than perovskite. However, as shown by recent estimations of partition coefficients (Corgne and Wood, 2005; Wu et al., 2009), perovskite shows little difference between the uptake of LREEs and HREEs. Therefore, as suggested by Mitchell and Reed (1988), crustal contamination after the crystallization of the perovskite can significantly decrease the La/Yb ratios of kimberlitic magma, since crustal materials have much lower La/Yb than perovskite. Therefore, the Mengyin kimberlite was not necessarily formed in a subduction setting although its source might contain some ancient oceanic lithosphere, as constrained by the Hf–Nd isotopes obtained from other kimberlites around the world.

What then controlled the formation of the Paleozoic kimberlites in the NCC? Before presenting our point of view, we need to briefly discuss the controversy concerning the source of kimberlitic magma in general. Mitchell (1995) proposed that the Group II kimberlites should be classified as orangeite, a specific type that is different from Group I kimberlite. As shown at Mengyin and globally, Sr–Nd–Hf isotopic data indicate that the mantle source is weakly depleted. This can reflect either a lithospheric (Heaman, 1989; Becker and Le Roex, 2006), or sub-lithosphere (Mitchell and Reed, 1988; Mitchell, 1995; Nowell et al., 2004; Gaffney et al., 2007) source. However, abundant evidence from mineral inclusions and experimental calibrations suggest that kimberlite is derived from the lower mantle (Moore and Gurney, 1985; Ringwood et al., 1992; Harte and Harris, 1994; Gasparik, 2000; Kerschhofer et al., 2000; Tachibana et al., 2006; Tappert et al., 2009), or at least affected by mantle plumes that originated from the core-mantle boundary (Haggerty, 1994, 1999).

Based on available data, it is unclear whether the Mengyin kimberlites are related to plume activity or not. However, the following lines of evidence support such a causal link. Firstly, the Mengyin and Fuxian kimberlites and their enclosed diamonds are reported to contain tungsten carbide (WC and WC_2) and natural Fe, Cu, Ag and Sn (Zhang et al., 1986; Leung, 1990; Dong, 1994; Chi and Lu, 1996). The former indicates a crystallization temperature of ~2800 °C (Chi and Lu, 1996), and the latter suggest an extremely reduced environment; both consistent with a deep mantle origin.

Secondly, Paleozoic kimberlites are widely distributed in the NCC. Besides Mengyin, kimberlites have been identified at Fuxian (Dong, 1994; Chi and Lu, 1996), at Tieling (Zhang, 1993; Chi and Lu, 1996; Wu et al., 2003), and several other places (Feng et al., 2000; Yang et al., 2002, Fig. 1). For the Mengyin kimberlite, our laser ablation analyses on perovskites give an age of 470 ± 4 Ma (Fig. 5). At Fuxian in Liaoning Province (Fig. 1), the lack of perovskite due to later alteration makes it impossible to precisely determine its emplacement age using the U–Pb method. However, it was previously reported that phlogopite from this kimberlite yields a Rb–Sr isochron age of 462 ± 5 Ma (Dobbs et al., 1994). Recently, a phlogopite Rb–Sr isochron age of 463 ± 7 Ma and an Ar–Ar age of 464 ± 6 Ma were reported (Li et al., 2005; Zhang and Yang, 2007). We therefore consider that the Mengyin and Fuxian kimberlites were emplaced coevally at ~470 Ma, which may also be the emplacement age of other kimberlites in the NCC, although they have not been precisely dated and further work is needed to verify this, especially since they do not contain diamonds.

Thirdly, the NCC was covered by a thick carbonate sedimentary sequence during the Cambrian–Early Ordovician. Since the Middle Ordovician (O_2), however, a gap of ~150 Ma duration is evident in the sedimentary record until the Middle Carboniferous (C_2), when terrestrial sediments were deposited with parallel unconformity (disconformity). Stratigraphic correlations from different localities indicate that uplift was initiated at the Early–Middle Ordovician boundary or in the early Middle Ordovician, at about 460–470 Ma, coeval with the emplacement of the Paleozoic kimberlites (Chen et al., 1997). Recent studies also indicate that the Korean Peninsula shows similar characteristics to the NCC at this time (Lee and Lee, 2003), marked by a lack of structural deformation and only vertical uplift over an area of >1,000,000 km^2. Although it has been argued that some kind of orogenic (epeirogenic?) process might be responsible for the uplift (Chen et al., 1997; Ma, 2002), the region does not show any sign of structural deformation or metamorphism. These features are all consistent with our proposal that a mantle plume was the likely trigger that initiated Early Paleozoic uplift in the NCC (see Campbell, 2007; Saunders et al., 2007). However, basaltic eruption is usually observed during plume activity, but is missing in the NCC during the early Paleozoic. One reason may be that the plume was not hot enough, although the vast area of uplift appears to contradict this. Alternately, the lithosphere may have been too thick to allow the plume head to rise high enough to trigger extensive melting of the shallow lithosphere, as documented by Griffiths and Campbell (1991) for the East African Plateau, where uplift was associated with alkali volcanism but no flood basalt volcanism. However, as stated by Ernst and Buchan (2003), more work is needed to verify the association of mantle plume activity with kimberlite emplacement, although this linkage is favored by many geologists (Moore and Gurney, 1985; Ringwood et al., 1992; Haggerty, 1994; Harte and Harris, 1994; Haggerty, 1999; Gasparik, 2000; Kerschhofer et al., 2000; Ernst and Buchan, 2003; Tachibana et al., 2006; Tappert et al., 2009).

6. Conclusions

(1) Perovskite in the Mengyin kimberlite has high Sr, Hf and REE concentrations. Its early crystallization during magmatic evolution makes it an ideal mineral to obtain the initial Sr, Nd and Hf isotopic ratio of kimberlitic magma. Conversely, the whole-rock isotopic data cannot be used to constrain the mantle source of kimberlite since it is subject to crustal contamination;

(2) Using the analytical protocol established herein, laser ablation analyses of Mengyin kimberlitic perovskite yields a narrow range of $^{87}Sr/^{86}Sr$ ratios from 0.70365 to 0.70381, with a weighted mean value of 0.70371 ± 12, identical to that obtained by the solution method, but much lower than the values obtained from whole-rock kimberlite samples. Laser ablation analyses establish that the perovskites have uniform, primitive

initial Nd isotopic compositions with a weighted average value of $\varepsilon_{Nd}(t)$ of 0.13 ± 0.22;

(3) Based on our U–Pb age and Sr–Nd–Hf isotopic data for perovskite, the Mengyin kimberlite was derived from a weakly depleted or primitive mantle source with an emplacement age of ~470 Ma, which is consistent with previously-documented evidence for regional uplift of the lithosphere in this area, close to the Early–Middle Ordovician boundary. The present weight of evidence supports the view that a mantle plume most likely triggered kimberlite activity in the NCC at this time.

Acknowledgements

We are grateful to Xian-Hua Li for providing the *Porites* sample, Larry Heaman for the Ice River samples and Peter Kinny for the TAZ samples. Frank C. Ramos kindly provided helpful suggestions during our ongoing analyses. Roberta Rudnick is thanked for her patience during our submission and resubmission over the past 2 years. Thoughtful and constructive comments by Amy Gaffney, Larry Heaman and an anonymous reviewer have substantially improved the manuscript. This study was supported by the Natural Science Foundation of China (Grants 40634019 and 40773008) and the Chinese Academy of Sciences.

Appendix A. Supplementary data

Supplementary data associated with this article can be found, in the online version, at doi:10.1016/j.chemgeo.2009.02.011.

References

Alibert, C., Albarede, F., 1988. Relationships between mineralogical, chemical, and isotopic properties of some North America kimberlites. Journal of Geophysical Research 93, 7643–7671.

Allsopp, H.L., Bristow, J.W., Smith, C.B., Brown, R., Gleadow, A.J.W., Kramers, J.D., Garvie, O.G., 1989. A summary of radiometric dating methods applicable to kimberlite and related rocks. In: Ross, J. (Ed.), Proceedings of the Fourth International Kimberlite Conference, v. 1, Kimberlites and Related Rocks: Their Composition, Occurrence, Origin and Emplacement. Geological Society of Australia Special Publication, vol. 14. Blackwell Scientific Publications, Oxford, pp. 343–357.

Balcaen, L., De Schrijver, I., Moens, L., Vanhaecke, F., 2005. Determination of the $^{87}Sr/^{86}Sr$ isotope ratio in USGS silicate reference materials by multi-collector ICP–mass spectrometry. International Journal of Mass Spectrometry 242, 251–255.

Batumike, J.M., Griffin, W.L., Belousova, E.A., Pearson, N.J., O, ' Reilly, S.Y., Shee, S.R., 2008. LAM–ICPMS U–Pb dating of kimberlitic perovskite: Eocene-Oligocene kimberlites from the Kundelungu Plateau, D. R. Congo. Earth and Planetary Science Letters 267, 609–619.

Becker, M., Le Roex, A.P., 2006. Geochemistry of South African on- and off-craton, Group I and Group II kimberlites: petrogenesis and source region evolution. Journal of Petrology 47, 673–703.

Becker, M., Le Roex, A.P., Class, C., 2007. Geochemistry and petrogenesis of South African transitional kimberlites located on and off the Kaapvaal Craton. South African Journal of Geology 110, 631–646.

Bizimis, M., Salters, V.J.M., Dawson, J.B., 2003. The brevity of carbonatite sources in the mantle: evidence from Hf isotopes. Contributions to Mineralogy and Petrology 145, 281–300.

Blichert-Toft, J., Albarede, F., 1997. The Lu–Hf isotope geochemistry of chondrites and the evolution of the mantle-crust system. Earth and Planetary Science Letters 148, 243–258.

Campbell, I.H., 2007. Testing the mantle plume. Chemical Geology 241, 153–176.

Chakhmouradian, A.R., Mitchell, R.H., 2000. Occurrence, alteration patterns and compositional variation of perovskite in kimberlites. Canadian Mineralogist 38, 975–994.

Chakhmouradian, A.R., Mitchell, R.H., 2001. Three compositional varieties of perovskite from kimberlites of the Lac de Gras field (Northwest Territories, Canada). Mineralogical Magazine 65, 133–148.

Chartier, F., Aubert, M., Salmon, M., Tabarant, M., Tran, B.H., 1999. Determination of erbium in nuclear fuels by isotope dilution thermal ionization mass spectrometry and glow discharge mass spectrometry. Journal of Analytical Atomic Spectrometry 14, 1461–1465.

Chen, J.B., Wu, T.S., Zhang, P.Y., You, W.C., 1997. Regional Stratigraphy of North China (in Chinese with English Summary). China University of Geosciences Press, Wuhan, pp. 45–64.

Chi, J.S., Lu, F.X., 1996. Kimberlites and the Features of Paleozoic Lithospheric Mantle in North China Craton. Science Press, Beijing. (in Chinese with English Summary) 292 pp.

Corgne, A., Wood, B.J., 2005. Trace element partitioning and substitution mechanisms in calcium perovskites. Contributions to Mineralogy and Petrology 149, 85–97.

Cox, R.A., Wilton, D.H.C., 2006. U–Pb dating of perovskite by LA–ICP–MS: an example from the Oka carbonatite, Quebec, Canada. Chemical Geology 235, 21–32.

Dobbs, P.N., Duncan, D.J., Hu, S., Shee, S.R., Colgan, E.A., Brown, M.A., Smith, C.B., Allsopp, H.P., 1994. The geology of Mengyin kimberlites, Shandong, China. In: Meyer, O.A., Leonardos, O.H., Gaspar, J.C. (Eds.), Kimberlites, Related Rocks and Mantle Xenoliths. Proceedings of the 5th International Kimberlite Conference, Araxá, Brazil, 1991, Companhia de Pesquisa de Recursos Minerais—CPRM Special Publication, Brasilia, 1A/93, pp. 40–61.

Dong, Z.X., 1994. Kimberlites in China. Science Press, Beijing. (in Chinese with English Abstract) 318 pp.

Dubois, J.C., Retali, G., Cesario, J., 1992. Isotopic analysis of rare earth elements by total vaporization of samples in thermal ionization mass spectrometry. International Journal of Mass Spectrometry and Ion Processes 120, 163–177.

Eggins, S.M., Kinsley, L.P.J., Shelley, J.M.G., 1998. Deposition and element fractionation processes occurring during atmospheric pressure sampling for analysis by ICP–MS. Applied Surface Science 127/129, 278–286.

Ehrlich, S., Gavrieli, I., Dor, L.B., Halicz, L., 2001. Direct high-precision measurements of the $^{87}Sr/^{86}Sr$ isotope ratio in natural water, carbonates and related materials by multiple collector inductively coupled plasma mass spectrometry (MC–ICP–MS). Journal of Analytical Atomic Spectrometry 16, 1389–1392.

Ernst, R.E., Buchan, K.L., 2003. Recognizing mantle plumes in the geological record. Annual Review of Earth and Planetary Sciences 31, 469–523.

Feng, C., Zhang, H.F., Zhou, X.H., 2000. New kimberlite field found in Liaoxi, China (in Chinese with English abstract). Seismic Geology 22 (supp.), 95–98.

Fortunato, G., Mumic, K., Wunderli, S., Pillonel, L., Bosset, J.O., Gremand, G., 2004. Application of strontium isotope abundance ratios measured by MC–ICP–MS for food authentication. Journal of Analytical Atomic Spectrometry 19, 227–234.

Foster, G.L., Vance, D., 2006. *In situ* Nd isotopic analysis of geological materials by laser ablation MC–ICP–MS. Journal of Analytical Atomic Spectrometry 21, 288–296.

Foster, G.L., Carter, A., 2007. Insights into the patterns and locations of erosion in the Himalaya — a combined fissiontrack and *in situ* Sm–Nd isotopic study of detrital apatite. Earth and Planetary Science Letters 257, 407–418.

Fraser, K.J., Hawkesworth, C.J., Erlank, A.J., Mitchell, R.H., Scott-Smith, B.H., 1985. Sr, Nd and Pb isotope and minor element geochemistry of lamproites and kimberlites. Earth and Planetary Science Letters 76, 57–70.

Gaffney, A.M., Blichert-Toft, J., Nelson, B.K., Bizzarro, M., Rosing, M., Albarede, F., 2007. Constraints on source-forming processes of West Greenland kimberlites inferred from Hf–Nd isotope systematics. Geochimica et Cosmochimica Acta 71, 2820–2836.

Gao, S., Rudnick, R.L., Carlson, R.W., McDonough, W.F., Liu, Y.S., 2002. Re–Os evidence for replacement of ancient mantle lithosphere beneath the North China Craton. Earth and Planetary Science Letters 198, 307–322.

Gasparik, T., 2000. Evidence for the transition zone origin of some [Mg, Fe]O inclusions in diamond. Earth and Planetary Science Letters 183, 1–5.

Griffin, W.L., Zhang, A.-D., O' Reilly, S.Y., Ryan, C.G., 1998. Phanerozoic evolution of the lithosphere beneath the Sino-Korean craton. In: Flower, M.F.J., Chung, S.L., Lo, C.H., Lee, T.Y. (Eds.), Mantle Dynamics and Plate Interactions in East Asia. Geodynamic Series, vol. 27. American Geophysical Union, Washington, D. C., pp. 107–126.

Griffin, W.L., Pearson, N.J., Belousova, E., Jackson, S.E., van Achterbergh, E., O' Reilly, S.Y., Shee, S.R., 2000. The Hf isotope composition of cratonic mantle: LAM–MC–ICPMS analysis of zircon megacrysts in kimberlites. Geochimica et Cosmochimica Acta 64, 133–147.

Griffiths, R.W., Campbell, I.H., 1991. Interaction of mantle plume heads with the Earth's surface and the onset of small-scale convection. Journal of Geophysical Research 96, 18295–18310.

Haggerty, S.E., 1994. Superkimberlites: a geodynamic window to the Earth's core. Earth and Planetary Science Letters 122, 57–69.

Haggerty, S.E., 1999. A diamond trilogy: superlumes, supercontinents, and supernovae. Science 285, 851–860.

Harte, B., Harris, J.W., 1994. Lower mantle mineral associations preserved in diamonds. Mineralogical Magazine 58A, 384–385.

Heaman, L.M., 1989. The nature of the subcontinental mantle from Sr–Nd–Pb isotopic studies on kimberlitic perovskite. Earth and Planetary Science Letters 92, 323–334.

Heaman, L.M., 2009. The application of U–Pb geochronology to mafic, ultramafic and alkaline rocks: an evaluation of three mineral standards. Chemical Geololgy. doi:10.1016/j.chemgeo.2008.10.021.

Heaman, L.M., Kjarsgaard, B.A., Creaser, R.A., 2003. The timing of kimberlite magmatism in North America: implications for global kimberlite genesis and diamond exploration. Lithos 71, 153–184.

Heaman, L.M., Kjarsgaard, B.A., Creaser, R.A., 2004. The temporal evolution of North American kimberlites. Lithos 76, 377–397.

Huang, J.Q., 1977. The basic outline of China tectonics (in Chinese). Acta Geologica Sinica 52, 117–135.

Isnard, H., Brennetot, R., Caussignac, C., Caussignac, N., Chartier, F., 2005. Investigations for determination of Gd and Sm isotopic compositions in spent nuclear fuels samples by MC ICPMS. International Journal of Mass Spectrometry 246, 66–73.

Jackson, S.E., Pearson, N.J., Griffin, W.L., Belousova, E.A., 2004. The application of laser ablation-inductively coupled plasma-mass spectrometry (LA–ICP–MS) to in-situ U–Pb zircon geochronology. Chemical Geology 211, 47–69.

Janney, P.E., Le Roex, A.P., Carlson, R.W., Viljoen, K.S., 2002. A chemical and multi-isotope study of the western Cape olivine melilitite province, South Africa: implications for the sources of kimberlites and the origin of the HIMU signature in Africa. Journal of Petrology 43, 2339–2370.

Jones, A.P., Wyllie, P.J., 1984. Minor elements in perovskite from kimberlites and distribution of the rare earth elements: an electron probe study. Earth and Planetary Science Letters 69, 128–140.
Kerschhofer, L., Schärer, U., Deutsch, A., 2000. Evidence for crystals from the lower mantle: baddeleyite megacrysts of the Mbuji Mayi kimberlite. Earth and Planetary Science Letters 179, 219–225.
Kinny, P.D., Griffin, B.J., Heaman, L.M., Brakhfogel, F.F., Spetsius, Z.V., 1997. SHRIMP U–Pb ages of perovskite from Yakutian kimberlites. Russian Geology and Geophysics 38, 97–105.
Kramers, J.D., Smith, C.B., 1983. A feasibility study of U–Pb and Pb–Pb dating of kimberlites using groundmass mineral fractions and whole-rock samples. Chemical Geology 1, 23–38.
Le Roex, A.P., Bell, D.R., Davis, P., 2003. Petrogenesis of Group I kimberlites from Kimberley, South Africa: evidence from bulk-rock geochemistry. Journal of Petrology 44, 2261–2286.
Lee, Y.I., Lee, J.I., 2003. Paleozoic sedimentation and tectonics in Korea: a review. The Island Arc 12, 162–179.
Leung, I.S., 1990. Silicon carbide cluster entrapped in a diamond from Fuxian, China. American Mineralogist 75, 1110–1119.
Li, Q.L., Chen, F.K., Wang, X.L., Li, X.H., Li, C.F., 2005. Ultra–low procedural blank and the single-grain mica Rb–Sr isochron dating. Chinese Science Bulletin 50, 2861–2865.
Liu, D.Y., Nutman, A.P., Compston, W., Wu, J.S., Shen, Q.H., 1992. Remnants of ≥3800 Ma crust in the Chinese part of the Sino-Korean Craton. Geology 20, 339–342.
Ludwig, K.R., 2003. ISOPLOT 3.0–A Geochronological Toolkit for Microsoft Excel. Berkeley Geochronology Center Special Publication. No. 4, 70 pp.
Luo, S.X., Ren, X.R., Zhu, Y., Chen, J.Z., Guo, Y.P., Wei, T.L., 1999. Geology of Shandong Diamond Deposits. Shandong Science and Technology Press, Jinan, pp. 1–136 (in Chinese with English Abstract).
Ma, L.F., 2002. Geological Atlas of China. Geological Publishing House, Beijing. (in Chinese) 348 pp.
McFarlane, C.R.M., McCulloch, M.T., 2007. Coupling of in–situ Sm–Nd systematics and U–Pb dating of monazite and allanite with applications to crustal evolution studies. Chemical Geology 245, 45–60.
Melluso, L., Lustrino, M., Ruberti, E., Brotzu, P., Gomes, C.B., Morbidelli, L., Morra, V., Svisero, D.P., D'Amelio, F., 2008. Major- and trace-element composition of olivine, perovskite, clinopyroxene, Cr-Fe-Ti oxides, phlogopite and host kamafugites and kimberlites, Alta Paranaiba, Brazil. Canadian Mineralogist 46, 19–40.
Menzies, M.A., Fan, W.M., Zhang, M., 1993. Palaeozoic and Cenozoic lithoprobe and the loss of >120 km of Archean lithosphere, Sino-Korean craton, China. In: Prichard, H. M., Alabaster, T., Harris, N.B.W., Neary, C.R. (Eds.), Magmatic Processes and Plate Tectonics. Geological Society Special Publication, vol. 76, pp. 71–81.
Mitchell, R.H., 1972. Composition of perovskite in kimberlite. American Mineralogist 57, 1748–1753.
Mitchell, R.H., 1986. Kimberlites: Mineralogy, Geochemistry, and Petrology. Plenum Press, New York. 442 pp.
Mitchell, R.H., 1995. Kimberlites, Orangeites, and Related Rocks. Plenum Press, New York. 410 pp.
Mitchell, R.H., Reed, S.J., 1988. Ion microprobe determination of rare earth elements in perovskite from kimberlites and alnoites. Mineralogical Magazine 52, 331–339.
Mitchell, R.H., Chakhmouradian, A.R., 1998. Instability of perovskite in a CO_2–rich environment: examples from carbonatite and kimberlite. Canadian Mineralogist 36, 939–952.
Moore, R.O., Gurney, J.J., 1985. Pyroxene solid solution in garnets included in diamond. Nature 318, 553–555.
Münker, C., Weyer, S., Scherer, E.E., Mezger, K., 2001. Separation of high field strength elements (Nb, Ta, Zr, Hf) and Lu from rock samples for MC–ICPMS measurements. Geochemistry Geophysics Geosystems 2. doi:10.1029/2001GC000183 (10.1029).
Nowell, G.M., Pearson, D.G., Bell, D.R., Carlson, R.W., Smith, C.B., Kempton, P.D., Noble, S.R., 2004. Hf isotope systematics of kimberlites and their megacrysts: new constraints on their source regions. Journal of Petrology 45, 1583–1612.
Paton, C., Hergt, J.M., Phillips, D., Woodhead, J.D., Shee, S.R., 2007a. New insights into the genesis of Indian kimberlites from the Dharwar Craton via *in situ* Sr isotope analysis of groundmass perovskite. Geology 35, 1011–1014.
Paton, C., Woodhead, J., Hergt, J., Phillips, D., Shee, S., 2007b. Sr–isotope analysis of kimberlitic groundmass perovskite via LA–MCICPMS. Geostandards and Geoanalytical Research 31, 321–330.
Pin, C., Zalduegui, J.F.S., 1997. Sequential separation of light rare-earth elements, thorium and uranium by miniaturized extraction chromatography: application to isotopic analyses of silicate rocks. Analytica Chimica Acta 339, 79–89.
Ramos, F.C., Wolff, J.A., Tollstrup, D.L., 2004. Measuring $^{87}Sr/^{86}Sr$ variation in minerals and groundmass from basalts using LA–MC–ICPMS. Chemical Geology 211, 135–158.
Richard, P., Shimizu, N., Allegre, C.J., 1976. $^{143}Nd/^{144}Nd$, a natural tracer: an application to oceanic basalts. Earth and Planetary Science Letters 31, 269–278.
Ringwood, A.E., Kesson, S.E., Hibberson, W., Ware, N., 1992. Origin of kimberlites and related magmas. Earth and Planetary Science Letters 113, 521–538.
Rocholl, A., Dulski, P., Raczek, I., 2000. New ID–TIMS, ICP–MS and SIMS data on the trace element composition and homogeneity of NIST certified reference material SRM 610–611. Geostandards Newsletter 24, 261–274.
Salters, V.J.M., White, W.M., 1998. Hf isotope constraints on mantle evolution. Chemical Geology 145, 447–460.
Saunders, A.D., Jones, S.M., Morgan, L.A., Pierce, K.L., Widdowson, M., Xu, Y.G., 2007. Regional uplift associated with continental large igneous provinces: the roles of mantle plumes and the lithosphere. Chemical Geology 241, 282–318.
Schmitz, M.D., Vervoot, J.D., Bowring, S.A., Patchett, P.J., 2004. Decoupling of the Lu–Hf and Sm–Nd isotope system during the evolution of granulitic lower crust beneath southern Africa. Geology 32, 405–408.
Simonetti, A., Heaman, L.M., Chacko, T., 2008. Use of Discrete-Dynode Secondary Electron Multipliers with Faradays — a 'Reduced Volume' Approach for In-Situ U–Pb Dating of Accessory Minerals Within Petrographic Thin Sections by LA–MC–ICP–MS. Mineralogical Association of Canada Short Course Series, vol. 40, pp. 241–264.
Smith, C.B., 1983. Pb, Sr and Nd isotopic evidence for sources of southern African Cretaceous kimberlites. Nature 304, 51–54.
Smith, C.B., Allsopp, H.L., Gravie, O.G., Kramers, J.D., Jackson, P.F.S., Clement, C.R., 1989. Note on the U–Pb perovskite method for dating kimberlites: examples from the Wesselton and De Beers mines, South Africa, and Somerset Island, Canada. Chemical Geology 79, 137–145.
Smith, C.B., Clark, T.C., Barton, E.A., Bristow, J.W., 1994. Emplacement ages of kimberlite occurrences in the Prieska region, southwest border of the Kaapvaal Craton, South Africa. Chemical Geology 113, 149–169.
Soderlund, U., Patchett, P.J., Vervoort, J.D., Isachsen, C.E., 2004. The ^{176}Lu decay constant determined by Lu–Hf and U–Pb isotope systematics of Precambrian mafic intrusions. Earth and Planetary Science Letters 219, 311–324.
Stacey, J.S., Kramers, J.D., 1975. Approximation of terrestrial lead isotope evolution by a two-stage model. Earth and Planetary Science Letters 26, 207–221.
Tachibana, Y., Kaneoka, I., Gaffney, A., Upton, B., 2006. Ocean–island basalt-like source of kimberlite magmas from West Greenland revealed by high $^{3}He/^{4}He$ ratios. Geology 34, 273–276.
Tappert, R., Foden, J., Stachel, T., Muehlenbachs, K., Tappert, M., Wills, K., 2009. Deep mantle diamonds from South Australia: a record of pacific subduction at the Gondwanan margin. Geology 37, 43–46.
Thirlwall, M., 1991. Long-term reproducibility of multicollector Sr and Nd isotope ratio analyses. Chemical Geology 94, 85–104.
Thy, P., Stecher, O., Korstgård, J.A., 1987. Mineral chemistry and crystallization sequences in kimberlite and lamproite dikes from the Sisimiut area, central West Greenland. Lithos 20, 391–417.
van Achterbergh, E., Ryan, C., Jackson, S., Griffin, W., 2001. Appendix 3, data reduction software for LA–ICP–MS. In: Sylvester, P. (Ed.), Laser-Ablation–ICPMS in the Earth Sciences. . Short Course Series, vol. 29. Mineral Association of Canada, pp. 239–243.
Vance, D., Thirlwall, M., 2002. An assessment of mass discrimination in MC–ICPMS using Nd isotopes. Chemical Geology 185, 227–240.
Vervoort, J.D., Patchett, P.J., Blichert-Toft, J., Albarede, F., 1999. Relationships between Lu–Hf and Sm–Nd isotopic systems in the global sedimentary system. Earth and Planetary Science Letters 168, 79–99.
Vervoort, J.D., Patchett, P.J., Soderlund, U., Baker, M., 2004. Isotopic composition of Yb and the determination of Lu concentrations and Lu/Hf ratios by isotopic dilution using MC–ICPMS. Geochemistry Geophysics Geosystems 5, Q11002. doi:10.1029/2004GC000721.
Vroon, P.Z., van der Wagt, B., Koornneef, J.M., Davies, G.R., 2008. Problems in obtaining precise and accurate Sr isotope analysis from geological materials using laser ablation MC–ICPMS. Analytical and Bioanalytical Chemistry 390, 465–476.
Wan, G., 1989. The distribution pattern of kimberlites and associated rocks in Shandong, China. In: Ross, J. (Ed.), Proceedings of the Fourth International Kimberlite Conference, v. 1, Kimberlites and Related Rocks: Their Composition, Occurrence, Origin and Emplacement. Geological Society of Australia Special Publication, vol. 14. Blackwell Scientific Publications, Oxford, pp. 401–406.
Wang, W.Y., Takahashi, E., Sueno, S., 1998. Geochemical properties of lithospheric mantle beneath the Sino-Korea craton; evidence from garnet xenocrysts and diamond inclusions. Physics of the Earth and Planetary Interiors 107, 249–260.
Wasserburg, G.J., Jacobsen, S.B., DePaolo, D.J., McCulloch, M.T., Wen, T., 1981. Precise determination of Sm/Nd ratios, Sm and Nd isotopic abundances in standard solutions. Geochimica et Cosmochimica Acta 45, 2311–2323.
Weis, D., Kieffer, B., Maerschalk, C., Pretorius, W., Barling, J., 2005. High-precision Pb–Sr–Nd–Hf isotopic characterization of USGS BHVO-1 and BHVO-2 reference materials. Geochemistry Geophysics Geosystems 6, Q02002. doi:10.1029/2004GC000852.
Weis, D., Kieffer, B., Maerschalk, C., Barling, J., Jong, J.D., Williams, G.A., Hanano, D., Pretorius, W., Mattielli, N., Scoates, J.S., Goolaerts, A., Friedman, R.M., Mahoney, J.B., 2006. High-precision isotopic characterization of USGS reference materials by TIMS and MC–ICP–MS. Geochemistry Geophysics Geosystems 7, Q08006. doi:10.1029/2006GC001283.
Weis, D., Kieffer, B., Hanano, D., Nobre, Silva, I., Barling, J., Pretorius, W., Maerschalk, C., Mattielli, N., 2007. Hf isotope compositions of U.S. Geological Survey reference materials. Geochemistry Geophysics Geosystems 8, Q06006. doi:10.1029/2006GC001473.
Williams, I.S., 1998. U–Th–Pb geochronology by ion microprobe. In: McKibben, M.A., ShanksIII III, W.C., Ridley, W.I. (Eds.), Applications of Microanalytical Techniques to Understanding Mineralizing Processes. Reviews in Economic Geology, vol. 7, pp. 1–35.
Woodhead, J.D., Hergt, J.M., 2001. Strontium, neodymium and lead isotope analyses of NIST glass certified reference materials: SRM 610, 612, 614. Geostandards Newsletter 25, 261–266.
Woolley, A.R., Bergman, S., Edgar, A.D., Le Bas, M.J., Mitchell, R.H., Rock, N.M.S., Scott Smith, B.H., 1996. Classification of the lamprophyres, lamproites, kimberlites, and the kalsilite-, melilite-, and leucite-bearing rocks. Canadian Mineralogist 34, 175–186.
Wu, F.Y., Walker, R.J., Ren, X.W., Sun, D.Y., Zhou, X.H., 2003. Osmium isotopic constraints on the age of lithospheric mantle beneath northeastern China. Chemical Geology 197, 107–129.
Wu, F.Y., Zhao, G.C., Wilde, S.A., Sun, D.Y., 2005a. Nd Isotopic constraints on the crustal formation of the North China Craton. Journal of Asian Earth Sciences 24, 523–545.
Wu, F.Y., Lin, J.Q., Wilde, S.A., Sun, D.Y., Yang, J.H., 2005b. Nature and significance of the Early Cretaceous giant igneous event in eastern China. Earth and Planetary Science Letters 233, 103–119.

Wu, F.Y., Yang, Y.H., Xie, L.W., Yang, J.H., Xu, P., 2006. Hf isotopic compositions of the standard zircons and baddeleyites used in U–Pb geochronology. Chemical Geology 234, 105–126.

Wu, F.Y., Zhang, Y.B., Yang, J.H., Xie, L.W., Yang, Y.H., 2008. Zircon U–Pb and Hf isotopic constraints on the Early Archean crustal evolution of the North China Craton. Precambrian Research 167, 339–362.

Wu, F.Y., Yang, Y.H., Mitchell, R.H., Zhang, Y.B., 2009. *In situ* U–Pb age determination and Nd isotopic analyses of perovskites from kimberlites in southern Africa and Somerset Island, Canada. Lithos in revision.

Xie, L.W., Zhang, Y.B., Zhang, H.H., Sun, J.F., Wu, F.Y., 2008. *In situ* simultaneous determination of trace elements, U–Pb and Lu–Hf isotopes in zircon and baddeleyite. Chinese Science Bulletin 53, 1565–1573.

Yang, J.M., Huang, Y.H., Qin, S.Y., Deng, C.J., Zhou, Z.X., Li, X.H., Zhang, L.X., Sui, P.S., 2002. Kimberlite and Lamproite in Northern Shanxi. Geological Publishing House, Beijing. (in Chinese with English Summary) 140 pp.

Yang, Y.H., Zhang, H.F., Xie, L.W., Wu, F.Y., 2007. Accurate measurement of neodymium isotopic composition using Neptune multiple collector inductively coupled plasma mass spectrometry (in Chinese with English abstract). Chinese Journal of Analytical Chemistry 35, 71–74.

Yang, J.H., Wu, F.Y., Wilde, S.A., Belousova, E., Griffin, W.L., 2008a. Mesozoic decratonization of the North China block. Geology 36, 467–470.

Yang, Y.H., Sun, J.F., Xie, L.W., Fan, H.R., Wu, F.Y., 2008b. *In situ* Nd isotopic measurement of geological samples by laser ablation. Chinese Science Bulletin 53, 1062–1070.

Yin, Z.W., Lu, F.X., Chen, M.H., 2005. SHRIMP age of exotic zircons in the Mengyin kimberlite, Shandong, and their formation. Acta Geologica Sinica 79, 654–661.

Yuan, H.L., Gao, S., Liu, X.M., Li, H.M., Gunther, D., Wu, F.Y., 2004. Accurate U–Pb age and trace element determinations of zircon by laser ablation–inductively coupled plasma mass spectrometry. Geostandards and Geoanalytical Research 28, 353–370.

Zhang, H.F., 1993. Discussion on geochemical characteristics and petrogenesis of kimberlites in Tieling, Liaoning province (in Chinese with English abstract). Geosciences 7, 458–464.

Zhang, H.F., Yang, Y.H., 2007. Emplacement age and Sr–Nd–Hf isotopic characteristics of the diamondiferous kimberlites from the eastern North China Craton. Acta Petrologica Sinica 23, 285–294 (in Chinese with English abstract).

Zhang, J.H., Yang, G.J., Li, Z.H., 1986. Discovery of natural tungsten carbide (WC) in China. Chinese Science Bulletin 6, 344–349.

Zhang, P., Hu, S., Wan, G., 1989. The distribution pattern of kimberlites and associated rocks in Shandong, China. In: Ross, J. (Ed.), Proceedings of the Fourth International Kimberlite Conference, v. 1, Kimberlites and Related Rocks: Their Composition, Occurrence, Origin and Emplacement. . Geological Society of Australia Special Publication, vol. 14. Blackwell Scientific Publications, Oxford, pp. 393–400.

Zhang, H.F., Goldstein, S., Zhou, X.H., Sun, M., Zheng, J.P., Cai, Y., 2008. Evolution of subcontinental lithospheric mantle beneath eastern China: Re–Os isotopic evidence from mantle xenoliths in Paleozoic kimberlites and Mesozoic basalts. Contributions to Mineralogy and Petrology 155, 271–293.

Zhao, G.C., Sun, M., Wilde, S.A., Li, S.Z., 2005. Late Archean to Paleoproterozoic evolution of the North China Craton: key issues revisited. Precambrian Research 136, 177–202.

Zheng, J.P., 1999. Mesozoic-Cenozoic Mantle Replacement and Lithospheric Thinning Beneath the Eastern China. China University of Geosciences Press, Wuhan. (in Chinese with English Abstract) 126 pp.